Circulation and stratification drivers during the summer season in the upwelling bay of Paracas (Peru): A modelling study

Cinthia Arellano, Vincent Echevin, Lander Merma-Mora, Adolfo Chamorro, Dimitri Gutiérrez, Arturo Aguirre-Velarde, Jorge Tam, François Colas

To cite this version:

Cinthia Arellano, Vincent Echevin, Lander Merma-Mora, Adolfo Chamorro, Dimitri Gutiérrez, et al.. Circulation and stratification drivers during the summer season in the upwelling bay of Paracas (Peru): A modelling study. Continental Shelf Research, 2023, 254, 10.1016/j.csr.2022.104923 . insu-03948245

HAL Id: insu-03948245
https://insu.hal.science/insu-03948245v1

Submitted on 8 Jan 2025

HAL is a multi-disciplinary open access archive for the deposit and dissemination of scientific research documents, whether they are published or not. The documents may come from teaching and research institutions in France or abroad, or from public or private research centers.

L'archive ouverte pluridisciplinaire **HAL**, est destinée au dépôt et à la diffusion de documents scientifiques de niveau recherche, publiés ou non, émanant des établissements d'enseignement et de recherche français ou étrangers, des laboratoires publics ou privés.

Distributed under a Creative Commons Attribution - NonCommercial 4.0 International License

Version of Record: https://www.sciencedirect.com/science/article/pii/S027843432200276X
Manuscript_80acbc3b02ee0e262e2f121c74c1efd7

Circulation and stratification drivers during the summer season in the upwelling bay of Paracas (Peru): a modelling study

Cinthia Arellano[1,2], Vincent Echevin[2], Lander Merma-Mora[3], Adolfo Chamorro[1], Dimitri Gutiérrez[1,3], Arturo Aguirre-Velarde[1], Jorge Tam[1], Francois Colas[2]

[1]Instituto del Mar del Peru (IMARPE), Esquina General Gamarra y Valle, Callao, Peru.
[2]LOCEAN-IPSL, IRD/Sorbonne Université/CNRS/MNHN, Paris, France.
[3] Laboratorio de Ciencias del Mar, Facultad de Ciencias y Filosofía, Centro de Investigación Para El Desarrollo Integral Y Sostenible (CIDIS), Universidad Peruana Cayetano Heredia, Lima, Peru.

Key Words: bay dynamics, upwelling, coastal wind, numerical modelling

Abstract:

The circulation and stratification in the shallow semi-enclosed bay of Paracas located downstream of the main upwelling cell off the Peruvian coast were studied during the summer season using a regional circulation model and in situ observations. A downscaling strategy based on a series of three embedded grids, from 10 km to 500 m resolution in the bay allows to take into account the influence of remote perturbations on the bay dynamics. Debiased surface winds from a high-resolution regional atmospheric model were used to force the model. The shortwave absorption depth was parameterized using satellite measurements of surface chlorophyll.

Sensitivity experiments to the model forcing and parameterizations were performed to investigate the impact of the wind diurnal variability, tidal forcing, freshwater discharge from a nearby river and shortwave absorption depth on the bay stratification. Results show that: debiasing the wind intensity reduced the model cold bias in the bay and increase the stratification; a shallow shortwave absorption depth induced a cooling of the subsurface water, increasing the stratification; freshwater discharge from the Pisco river north of the bay increased slightly the stratification in the bay during days of weak wind. The high sensitivity of the bay stratification to the atmospheric forcing calls for the need to use more realistic wind forcing products.

The circulation in the bay under strong (> 5.5 m s^{-1}) and weak (< 3 m s^{-1}) winds was also examined. The summer circulation during strong upwelling-favorable wind conditions was characterized by northward surface currents transporting the bay surface waters outward and subsurface currents transporting cold deeper waters into the bay along its western shore. During weak wind conditions, the current is outward in the bottom layer and a surface southward current related to the poleward

© 2022 published by Elsevier. This manuscript is made available under the CC BY NC user license
https://creativecommons.org/licenses/by-nc/4.0/

undercurrent flowing over the continental slope and shelf transported warm waters into the bay, generating a cyclonic circulation in the bay.

1. Introduction

Coastal bays have particular features that may modify wind orientation and strength and generate complex circulation patterns of the water masses within and around them. In Eastern upwelling systems, coastal upwelling is driven by the alongshore wind, generating offshoreward Ekman transport of the surface waters and vertical transport of cold and nutrient replete subsurface waters. Coastal regions with linear coastlines are not very favorable to ecological productivity as plankton-rich waters are transported offshore. In contrast, upwelling bays, depending on the nearby coastal orography, bay dimensions, bottom topography and water stratification, may harbor so-called upwelling shadows which are regions of surface waters recirculation and retention, favorable to plankton development and larvae survival (Largier, 2020). Furthermore, upwelling near coastal headlands upwind of the bays are generally enhanced, leading to an upwelling jet separating from the coast.

Paracas bay is a small (L~5 km), roughly square and shallow (<15 m depth) bay facing north, located within the upwelling bay of Pisco off South-Central Peru (13.8°S; **Figure 1**). It is bordered to the west by a low headland (the Paracas peninsula) creating a wind decrease and onshoreward direction change downwind of the headland. Approximately 15 km north of the bay, the Pisco river discharges mainly during austral summer. This upwelling bay is located downstream of one of the main upwelling cells of the very productive Peruvian Upwelling System (hereafter PUS; Chavez et al., 2008).

As other coastal embayments in the PUS (*e.g.* Sechura bay, 5.5°S; Flores et al., 2019; Independencia bay, 14.2°S; Taylor et al., 2008) and along the Chilean coast (Tongo bay, 30°S; Lagos et al., 2016; Arauco bay, 37°S; Valle-Levinson et al., 2003), Paracas bay undergoes a strong anthropogenic pressure: traditional scallop (*Argopecten Purpuratus*) aquaculture takes place in the bay, and artisanal and industrial landings of anchovy in Pisco harbour north of the bay amount to ~10% of the total Peruvian landings. Fish meal factories (transforming anchovy into oil and flour) in the Pisco area discharge huge amounts of fish waste through a submarine emissary (at 50 m depth) north of Paracas bay, possibly playing a role in the triggering of extreme events such as HABs (Cabello et al., 2002; Cuellar-Martinez et al., 2021). On the other hand, tourism in the Paracas National Reserve reached close to one million tourists in 2019 (El Comercio, 2019).

Upwelling bay ecosystems may also be strongly impacted by extreme events due to various natural forcings. During El Niño events (*e.g.* Barber and Chavez, 1983; Colas et al., 2008) warm waters of tropical origin flowing southward along the Peruvian coast may flow into Paracas bay, enhance stratification and reduce mixing between surface ventilated waters and subsurface oxygen-deficient waters (Aguirre et al., 2019; Merma-Mora et al., 2022). Episodic offshore upwelling and transport into the bay of subsurface nearly-anoxic waters from the offshore oxygen minimum zone (Aguirre et al., 2019; Merma-Mora et al., 2022; Lagos et al., 2016 in Tongo bay), as well as intense respiration of organic matter following HABs (Kahru et al., 2004) may trigger anoxia and generate mass mortality of scallops and fish in the bay (Cueto-Vega et al 2021; Cabello et al., 2002). Also, periods of anoxia may be followed by so-called “white water” events associated with sulfide oxidation (Schunck et al., 2013; Ohde, 2018; e.g. Lavik et al., 2008 near Walvis bay, 23°S, over the south African shelf), leading to fish and scallop mortality, as well as nasty smell and other impacts on human activities around the bay.

Such biogeochemical events related to a weak ventilation of subsurface waters can be generated by (i) strong stratification/weak vertical mixing in the bay or/and by (ii) the upwelling of oxygen-depleted offshore source waters into the bay. Stratification in the shallow south-western part of the bay (5m depth; **Figure 1b**) during austral spring-summer 2012-2013 displays a high variability at daily to seasonal time scales, with low values (~ 0-0.2 σ unit m^{-1}) during spring and high values (~1 σ unit m^{-1}) in summer in particular during periods of weak winds (Aguirre et al., 2019). The latter also coincide with the southward transport of freshwater from the Pisco river in the bay.

As for many other bays, the dynamical processes driving the stratification and the circulation patterns in Paracas bay area are not well known, due to a lack of measurements and to short-duration shipboard surveys. Tentative circulation schemes have been proposed based on several short-duration surveys conducted by the Instituto del Mar del Peru (IMARPE). Guzmán et al. (1997) sketch very complex surface and subsurface circulation patterns from a dozen ADCP measurement points in late May 1996. Using ADCP measurements collected over a few days in different months, Sanchez et al. (2019) describe contrasted surface circulation patterns in and north of the bay: during weak wind conditions in April 2013, the surface circulation was poleward all over the bay, whereas during moderate upwelling-favorable wind conditions (November 2014 and March 2015) the flow was southward along the western side of the bay and northward along the eastern side. On the other hand, during the strong 2015-16 El Niño and in spite of strong upwelling-favorable winds in July 2015, southward surface flow was measured along the eastern side of the bay, in accordance with the predominant poleward alongshore currents associated with a downwelling coastal wave during that period. Last, Moron et al. (2017) characterized the physical environment north of the bay during October 2013. They found weak surface currents near the coast and mainly westward surface currents offshore. At 5-10 m depth, the circulation north of the bay mouth was mainly northward. Overall, even though these studies provide a glimpse of the complex circulation in the bay area under various wind regimes and large-scale circulation conditions, the absence of long-term, high-frequency measurements precludes a clear representation of the bay area circulation at daily to seasonal time scales.

In contrast to upwelling bays in other EBUS (e.g. Drake et al. (2018) for Monterey bay in the California upwelling system; Penven et al. (2000) for St Helena bay in the Benguela upwelling system), few modelling studies have been carried out to study upwelling bays in the PUS. To our knowledge, only two modelling studies focused on the study of circulation patterns in Paracas bay. Carbonel (2013) used a two-layer reduced gravity model with a horizontal resolution of 450 m and a realistic topography and coastline to investigate the short-term (~7 days) circulation and density structure in response to the southwesterly-westerly winds in the bay. Such wind regime forced an upwelling of relatively cold waters (~16°C) along the western side of the bay and a sluggish southward circulation in the bay. A downwelling occurred in the eastern part of the bay and in a coastal band north of the bay, leading to higher surface temperatures (~20-21°C). On the other hand, Quispe-Sánchez (2007) used the three-dimensional primitive equations Estuary and Lake Computer Model (ELCOM, Hodges et al., 2000) with a realistic bottom topography and horizontal resolution of 100 m to study the circulation and stratification in the bay during a time period of 5 days (May 14-19th 2005). The model was forced by observed winds and heat fluxes from the Pisco airport (see **Figs 2b,d**) and by sea level tidal elevation at the open boundaries. He found that, under upwelling-favorable winds, cold water filled the bottom in the western part of the bay, increasing stratification. Furthermore, the wind forcing modulated the surface currents (~2-5 cm s^{-1}) while tidal forcing appeared to modulate the subsurface currents (~2-3 cm s^{-1}). Bay-scale cyclonic surface circulation patterns were found due to the interaction between wind-forced and tidal currents. In conclusion, these modelling studies provided information on the circulation and stratification in Paracas bay over very short time periods (a few days) in relatively idealized modelling frameworks. Thus, several questions remain to be addressed to better understand the dynamics of Paracas bay: what are the dynamical forcings (wind, heat fluxes, tides, runoff and large scale circulation) controlling the stratification in the bay from diurnal to intraseasonal time scales? What are the circulation patterns in the bay forced by the wind synoptic variability?

In the following, we investigate the dynamical drivers of the stratification and circulation in Paracas bay from diurnal to intraseasonal time scales during the summer season. An elaborate, realistic modelling framework based on embedded model grids of increasing spatial resolution (e.g. Mason et al., 2010) is used. This downscaling approach allows taking into account the effect of the the inner shelf circulation (north of the bay) on the bay dynamics, in particular the influence of the southward undercurrent occasionally reaching the surface and flowing into the bay. Focus is given on the austral summer season (January-March) during which the large stratification may lead to subsurface hypoxia in the bay (Aguirre et al., 2019; Merma-Mora et al., 2022) with important consequences on the ecosystem. Different dynamical forcings (wind synoptic variability, wind diurnal cycle, tidal forcing, freshwater discharge, see section 2.4) and model parameterizations (see section 2.5) are used to investigate their respective impact on the sea surface temperature patterns, thermal/density stratification and circulation in the bay area. A similar modelling sensitivity study of the dynamical forcings impacting stratification in a shallow lagoon system has been done recently by Kang and Xia (2022).

Section 2 details the modelling strategy, the forcings and observations used. Section 3 presents the results of the model experiments: the model biases as well as the impacts of various parameterizations and forcings on the stratification in and north of the bay are described. Lastly, the time-averaged circulation in the bay area is characterized over the whole summer season and during periods of strong (>5.5 m s^{-1}) and weak(< 3 m s^{-1}) winds within the season. Sections 4 and 5 present a discussion and the conclusions and perspectives of the study, respectively.

2. Material and Methods

2.1 The CROCO regional model

The Coastal and Regional Ocean Community Model (CROCO, Hilt et al., 2020) is used to simulate the ocean dynamics in Paracas bay. This model is a new generation regional ocean circulation model, mainly based on an evolution of the Region Ocean Model System (ROMS-AGRIF; Shchepetkin and McWilliams, 2009). The CROCO code is based on the Boussinesq approximation and on the hydrostatic balance to solve the Reynolds-averaged Navier Stokes equations. The model uses a split-explicit time-stepping and stretched terrain-following sigma coordinates in the vertical and the Arakawa-C grid on the horizontal. A third-order upstream biased advection scheme is used for the horizontal advection of momentum and tracers. The Generic Length Scale (GLS) and K-profile parameterization (KPP) were both tested for subgrid scale vertical mixing. A linear bottom friction (with a drag coefficient of 3.10^{-4} s^{-1}) is used. Bulk formulae from Fairall et al. (2003) were used to compute atmospheric heat and momentum fluxes.

2.2 The Paracas model configuration

A one-way offline nesting strategy based on the “ROMS2ROMS” downscaling (Mason et al., 2010) was set up to study the circulation in the bay. Three embedded model grids are used, and the boundary conditions from the largest domain are provided to the smaller domain. The largest grid (named D01 in the following) has a horizontal resolution of ~ 10 km and covers the whole PUS and the eastern part of the offshore Equatorial Current System, from 5ºN to 22ºS and from 95ºW to 70ºW (**Fig.1a**). The D01 grid extent allows to take into account (i) the effect of the eastward near-equatorial jets on the nearshore circulation, in particular on the Peru-Chile Under Current (hereafter PCUC; *e.g.* Montes et al., 2010) and (ii) the effect of the southward propagating coastal trapped waves on the shelf circulation (*e.g.* Colas et al., 2008; Echevin et al., 2014).

The second domain (D02) has a resolution of ~ 2.5 km, covers the PUS from 3°S to 16°S, and uses daily outputs of D01 as boundary conditions. D02 simulates the mesoscale dynamics that forces the local dynamics in the third grid. Bottom topography from the Shuttle Radar Topography Mission (STRM30, Rodriguez et al., 2005) is used for D01 and D02 grids.

The third and smallest domain (D03, ~ 500 m resolution) is centered on Paracas Bay. It is forced by daily outputs of D02 at its northern and western boundary. A local, high resolution (50 m) bottom topography gridded product (Chacon, 2014) is used for D03. The minimum depth is 5 m.

Each domain has 32 vertical levels, with a higher concentration of levels in the surface layer (with sigma-coordinates parameters thetas=6, thetab=0, see https://www.croco-ocean.org/ for details on the vertical grid discretization).

2.3 Datasets for model forcing and evaluation

Datasets used for model forcing

Physical variables (temperature, salinity, currents and sea level) from the Mercator 1/4º (~ 25km) ocean reanalysis were used for the open boundary conditions (OBC) of the largest domain D01. Mercator model (GLOBAL_REANALYSIS_PHY_001_025) output is freely available at https://datastore.cls.fr/catalogues/eu-copernicus-marine-service-global-reanalysis-glorys/. This reanalysis simulates the recent period (1993-2015) during which altimeter and ARGO data are assimilated. Details about the Mercator reanalysis (ocean model configuration, atmospheric forcings and assimilation procedures) can be found in Lellouche et al. (2013). This product provides daily averages of sea level, temperature, salinity and velocity at 75 vertical levels (from the surface to 5500 m depth). A monthly climatology of these variables over the 2008-2015 was used for D01 in the sensitivity experiments presented below. The variables were interpolated onto D01 grid open boundaries using the ROMSTOOLS package (Penven et al., 2008).

Sea level, barotropic zonal and meridional currents from the TPXO7 global tidal model were used to force the tidal signal in D03. TPXO7 is a global ocean tidal model which best-fits, in a least-squares sense, the Laplace tidal equations and altimetry data (Egbert and Erofeeva, 2002). The tidal forcing is provided as complex amplitudes of sea-surface elevation and barotropic velocity for eight primary components (M2, S2, N2, K2, K1, O1, P1, Q1) and two long tidal period components (Mf, Mm). TPXO7 values are interpolated over the D03 domain boundaries using the ROMSTOOLS package (Penven et al., 2008).

Surface winds (10 m) from the Advanced Scatterometer (ASCAT) at 0.25°x0.25° resolution (Bentamy and Fillon, 2012) were used for D01 and D02 wind forcing. Nearshore surface winds at 7 km resolution (available every 6 h) from a regional atmospheric simulation with the Weather Research and Forecasting model (WRF, Skamarock and Klemp, 2008) over the Peru region (Chamorro et al., 2021) were used to correct ASCAT wind nearshore bias in D01 and D02 (see section 2.4a). Debiased WRF winds were used for D03 (see section 2.4b). The WRF simulation reproduced the mean state and seasonal variability of coastal wind off Peru with a fair degree of realism over the period 1994-2003. Details on the WRF model set up can be found in Chamorro et al. (2021).

Wind speed data from the Meteorological Aerodrome Reports (METAR) of the Pisco airport meteorological station (8 m above ground) was used to evaluate the wind diurnal variability. Since this station is located less than 1 km from the seashore in a zone devoid of major orographic obstacles, it was considered as a proxy of the surface wind intensity within the bay.

Monthly climatologies (2008-2015 period) of air temperature, humidity and precipitation from ERA-interim (Berrisford et al. 2011) were used for the three domains. Downward longwave radiation from the 1°x1° resolution TropFlux product (Kumar et al., 2012) was used. Shortwave radiation from TropFlux, Objectively Analyzed air-sea fluxes (OAFLUX, Jin and Weller, 2008), COADS (Da Silva et al., 1994) were compared to local observations from the Sutron coastal station (13.8°S, 76.28°W; 2010-2013 time period; see section 2.4c) operated by the National Service of Meteorology and Hydrology of Peru (SENAMHI).

SeaWIFs satellite data (O'Reilly et al., 1998) at ~9 km resolution from September 1997 to December 2008 were used to compute a monthly climatology of surface chlorophyll concentration to compute chlorophyll-dependent water types and shortwave absorption depth varying in time and space (see Sec. 2.5.b).

The Pisco river runoff was measured at a hydrological station located 60 km upstream from the river mouth by the Peruvian National Water Authority (ANA), and was used as a proxy for the river discharge north of the bay

Data sets used for D03 model evaluation

Tide gauge sea level at Pisco station (13.417ºS,76.133ºW) available for the period 1999 to 2014 (http://uhslc.soest.hawaii.edu/data/?rq) was used to evaluate the model tidal signal. To extract the tidal signal from the tide gauge and CROCO model time series, we used the "t_tide" filtering algorithm (Pawlowicz et al., 2002) to hourly time series.

In situ temperature and salinity from 16 stations were used to evaluate the model spatial patterns and stratification (**Fig. 1b**). The stations were sampled at least once a month between 2010 and 2015 by the IMARPE-Pisco Coastal Laboratory. Surface and bottom (1 m above seafloor) temperature and salinity were measured using a mercury thermometer and a Portasal Salinometer 8410A. A monthly climatology for the period 2010-2015 was computed for each station and depth. Density was computed using the non-linear equation of state from Jackett and McDougall (1995).

Two temperature time series were also used: a time series from the "Terminal Marino Pisco Camisea" was collected north of the bay (P1, 13.70ºS, 76.35ºW, **Fig.1b**). The measurements were collected once a day over 2006-2016. The temperature was measured at 0, 5, 10 and 15 m depth. A climatology of the temperature data (**Fig.5a**) was used to evaluate the model. Hourly time series (September 2012-March 2013) of bottom (~4m depth) and ~2 m depth temperatures from a fixed point in the south western shallow part of the bay (P2, 13.82º, 76.29º, **Fig. 1b;** Aguirre et al., 2019) was used to evaluate the thermal diurnal cycle over the summer period (January-March 2013; **Fig.5b**).

2.4 Atmospheric and river forcing methodology

a. Correction on ASCAT wind for D01 and D02 forcing

Due to their relatively low spatial resolution (0.25°) and lack of data in a coastal band known as the “coastal blind zone” (**Fig.2a**), ASCAT gridded winds need preprocessing before they can be used to force a high-resolution regional model. Indeed, the wind decreases shoreward, a characteristic known as “wind drop-off”, which mainly occurs in the blind zone of the satellite (see Fig.4 in Chamorro et al., 2021). This can result from SST-wind interaction and orographic or coastline effects (*e.g.* Boé et al. 2011; Renault et al., 2016 in the California EBUS). This wind drop-off plays an important role in coastal upwelling: a strong drop-off favors offshore Ekman pumping, while a weak drop-off (i.e. strong nearshore wind) favors an intense and localized coastal upwelling (Capet et al., 2004). Using along-track altimeter derived surface wind speed close to the coasts, Astudillo et al. (2017) confirmed the presence of a nearshore wind drop-off off Peru. Because of missing data in the “coastal blind zone”, a linear interpolation is routinely done to extrapolate offshore wind values onto the nearshore ocean grid points, which keeps the wind almost constant between ~ 30 km offshore and the coastline. Because of this artifact, the D01 SST in the coastal band was colder (~ 1°C, Figure not shown) than observations. This prompted us to modify the coastal wind profiles to alleviate this cold bias. The correction applied for D01 and D02 wind fields is described below.

- For D01 correction, we used a monthly climatology (over the period 1994-2003) of the WRF wind field to compute the wind intensity reduction $r(x,y)=[w(x,y)-w(x+dx,y)]/w(x,y)$ for each longitude x (from offshore (x=-60) to nearshore (x=0) in a 60 km-wide coastal band) and each latitude y between 6°S and 14°S. The space-dependent reduction was then applied to the ASCAT wind intensity (w_{ascat}), as follows:

$$w'(x+dx,y)=w'(x,y) * (1-r(x,y))$$

with the offshore boundary condition: $w'(-60,y)= w_{ascat}(-60,y)$.

The corrected wind displayed a greater nearshore drop-off than the ASCAT extrapolated data (see **Fig.S1**). Note that the wind direction was not modified.

- The same method was applied for the D02 domain: the corrected wind for the D01 domain and WRF winds were first interpolated over D02 (2.5 km resolution). Then, a similar drop-off correction was applied to construct the D02 wind forcing.

b. Correction of WRF wind for D03 forcing

WRF winds are used for D03 domain as its eastern part is located within the ASCAT blind zone (**Fig. 2**; note that there is only one WRF grid point located in Paracas bay). To evaluate the realism of WRF winds in the bay area, we compared the seasonal cycle of the observed wind at Pisco Airport and of the modelled wind (**Fig. 2d**). We also compare the seasonal cycle of ASCAT and WRF winds at an offshore location west of the bay (**Fig. 2c**). The seasonal variability differs in the bay and offshore: winds are stronger during summer in the bay (**Fig.2d**), whereas offshore winds are stronger during winter (**Fig.2c**) due to the equatorward migration of the South Pacific anticyclone. WRF winds represent relatively well the observed seasonal variability in both locations, with an overestimation of the wind intensity.

In order to take into account the role of the intraseasonal wind variability on the bay ocean dynamics, we used the WRF daily winds (hereafter WRF_{2003}^{d}) of the summer 2003. This particular year was selected because of its weak interannual variability (i.e. neutral El Niño period). Then, in order to filter the remaining interannual variability in 2003, the monthly mean anomalies for 2003 (WRF_{2003}^{m}) were subtracted to the 2003 daily time series to obtain intraseasonal wind variability (daily to weekly) of summer 2003. The latter (i.e. left term in the equation below) was then added to the WRF monthly climatology over the period 1994-2003 (WRF_{clim}^{m}), as follows:

$$WRF'(t)= WRF_{clim}^{m}(t) + [\, WRF_{2003}^{d}(t) - WRF_{2003}^{m}(t) \,]$$

After subtracting the interannual variability, the corrected daily wind field WRF' is typical of any summer season, except for the remaining intraseasonal variability corresponding to 2003. After this processing, the offshore wind values of WRF'(t) remained too high with respect to ASCAT winds (**Fig. 2c**), leading to overly strong upwelling and cold SST in the bay area (Figures not shown). To scale WRF'(t) with the offshore ASCAT wind intensity, a monthly time-varying correction factor F(t) was computed as the ratio between the ASCAT and WRF' maximum wind speed values in an offshore box (13°S-15°S;78.5°W-76°W). WRF'(t) was then multiplied by F(t) to obtain the corrected wind (WRF^{*}) used to force D03.

c. **Correction of the net downward shortwave flux bias in D03:**

Various climatologies of net downward shortwave flux were compared to a climatology of local observations from a coastal station (13.8°S,76.28°W, see section 2.3) over the period 2010-2013 (**Fig. 3)**. In summer, TROPFLUX and OAFLUX fluxes were respectively ~30 W m^{-2} and ~15 W m^{-2} lower than the local flux, whereas COADS flux was ~ 20-30 W m^{-2} higher. The TROPFLUX product was corrected by adding a constant value of +30 W m^{-2} over the whole D03 domain, which reduced the model SST cold bias (Figure not shown). This correction is used in all the simulations described below. Note that diurnal shortwave variability is parameterized in the model using an analytical diurnal cycle (**Fig.4b**) superimposed on the daily-mean values.

d. **River runoff**

A monthly climatological river discharge is used in one simulation (Sec. 2.7; Table 1). It is introduced over two D03 grid points located at the Pisco river mouth (**Fig.1b**). The salinity and temperature of the discharge water are set to 17°C and 10 psu respectively and do not vary in time over the summer period. The vertical profile of the discharge flux is depth-independent.

2.5 Model parameterizations

a. Diurnal variability of the wind intensity

When used, the diurnal variability of the wind intensity was parameterized online, by modulating analytically the daily-mean wind intensity (**Fig. 4a**). A third degree polynomial function was best-fitted to the observed diurnal value, and multiplied to the daily mean value for each model time step. The direction of the wind was kept constant during the day.

b. Sea water absorption of shortwave flux

The sea water type, which depends on the water turbidity, determines how the incoming shortwave solar radiation is absorbed in the upper layer of the water column, therefore it may play an important role in the stratification characteristics. A parameterization by Paulson and Simpson (1977) based on Jerlov (1976) optical water types is implemented in CROCO: five different Jerlov water types are considered, from type 1 (used by default in most CROCO simulations, see Echevin et al., 2021) which represents clear water, to type 5 which represents turbid water. Ranges of chlorophyll values can be associated with the water types (Paulson and Simpson, 1977), with low concentrations (<0.01 mg Chl m^{-3}) for type 1 and high concentrations (1.5- 2 mg Chl m^{-3}) for type 5. The seasonal concentrations of surface chlorophyll in the bay area are high (**Fig. S2**) leading to a water type 5 in and north of the bay and to water type 4 offshore. In the base case simulation (see Table 1), water type 1 is used in the whole domain.

2.6 Boundary conditions

In order to investigate the typical summer dynamics of the bay, it is necessary to avoid strong interannual oceanic variability propagating from the equatorial region. Thus a 10-year climatological D01 simulation forced by monthly climatological boundary conditions from Mercator (see section 2.3) and climatological ASCAT corrected wind (see section 2.4a) was performed. Daily outputs from the last seven years of the simulation were used as boundary conditions for a seven-year D02 climatological simulation. Daily outputs from the last 2 years of this D02 simulation were used to force the D03 grid. Note that in the present study, sensitivity experiments (see Section 2.7) are performed using only the boundary forcing from the first of these last two years of the D02 simulation.

2.7 Simulation characteristics

A series of simulations were performed to evaluate the effect of the different physical forcings, wind bias corrections, and model parameterizations on the summer stratification in the bay:

- The “Base case” simulation (named D03-A) is forced by uncorrected WRF daily winds and corrected shortwave fluxes. Vertical mixing is parameterized using GLS. Corrected shortwave fluxes and GLS mixing are also used in the other experiments unless mentioned otherwise.
- The diurnal wind variability (see section 2.5a) which may modify mixed layer properties and rectify intraseasonal variability (Bernie et al., 2005) was implemented in the experiment D03-B wind forcing. Other parameterizations and forcings are similar to those of D03-A.
- The impact of chlorophyll-related turbidity on the shortwave flux downward penetration (see section 2.5b) was evaluated in simulation D03-C. Other parameterizations are similar to those of D03-B.
- The tidal forcing was introduced in simulation D03-D.
- The WRF wind speed correction (see section 2.4.b) was introduced in simulation D03-E.
- The Pisco river discharge was introduced in D03-G.
- The combined influences of diurnal wind variability, chlorophyll-related shortwave absorption depth and wind correction were evaluated in simulation D03-I.

The simulations characteristics are summarized in Table 1.

2.8 **Metrics**

In this section, we analyze the effect on the bay thermal stratification produced by each forcing and parameterization listed in section 2.7. To evaluate the model simulations in the bay area, our main metrics are the comparison between the modeled and observed: (i) climatological sea surface temperature, (ii) near-bottom temperature and stratification (surface-bottom density, see **Table 3**) time series at P1 and P2, and (iii) summer climatological stratification (surface minus bottom density) at 16 stations in the bay (see locations in Figure 1). Using the latter, mean bias and root mean squared error (RMSE) are also computed (see **Table 2**).

3. Results

3.1 Evaluation of D01 and D02 climatological simulation

The surface temperature, cross-shore temperature structure, and alongshore mean current patterns from D01 and D02 simulations were evaluated in the Peruvian coastal region. As the coastal dynamics over the whole Peru shelf is not the focus of our paper, a brief summary of the results is given in this section and figures are shown in the supplementary material.

The D01 mean SST displays a coastal band of relatively cold water (~16°C) and warmer (~20-24°C) water offshore typical of EBUS (**Fig.S3**). A moderate cold bias (~1°C) is found near the coast, owing to the nearshore wind correction (see section 2.4a). North of the bay (~13.5°S), the D02 cross-shore mean thermal structure displays an isotherms shoaling towards the coast, typical of coastal upwelling (**Fig.S4**). The modeled isotherms slopes are slightly too steep with respect to the observations, leading to a near-surface cold bias near the coast (~1°C). The D02 alongshore circulation (averaged between 7°S and 13°S) is in good agreement with the observations (Chaigneau et al., 2013), with maximum poleward velocity of ~8 cm/s (~ 11 cm/s in the observations) over the slope near ~100 m depth (**Fig.S5**). Overall, the good agreement between observed and modeled features shows that our downscaling approach is an efficient tool to study the nearshore ocean dynamics in the region of interest.

3.2 Impact of forcings and parameterizations on the stratification in the bay area

a. Observations north of the bay (P1)

At P1 the mean surface (1m depth) temperature is ~20ºC during summer and ~16ºC during winter (**Fig.5a**). The mean bottom temperature (15m depth) displays a different seasonality, with a minimum (~15°C) in October-November and a maximum (~17°C) in June. Time series for a particular year (2006) are also shown as an example to highlight the pronounced intraseasonal variability. The thermal stratification (i.e. the difference between the surface and bottom temperature, not shown) varies between ~3.6ºC and ~0.7°C in summer and winter respectively. Due to the lack of salinity measurements at P1, a constant (in time and over the vertical) salinity (35 psu) was used to compute the density stratification (0.89 kg m^{-3} and 0.16 kg m^{-3} in summer and winter, respectively). In the following sections, the focus is on the stratified summer season.

b. Base case simulation

The starting point of our study is the evaluation of the base case simulation D03-A, forced by daily-mean WRF winds (see **Table 1**). The model summer SST displayed a meridional pattern, with nearshore warm waters (~20-24°C) north of the bay and cold waters (~18-19°C) in the bay (**Fig.6a**). The coldest surface waters (~18°C) were found north of the Paracas peninsula, likely related to offshore upwelling. While the model nearshore SST was close to the observed north of the bay, a cold bias of ~1.5-2ºC was found offshore and in the bay.

Model bottom temperatures ranged between 15-16°C offshore at 50-60 m depth and 19-20°C nearshore at ~5 m depth (**Fig.6b**). The observed bottom temperatures tended to be slightly lower (by ~1°C) than the modeled ones, particularly near the western side of the bay mouth where subsurface waters entered the bay during phases of coastal upwelling (see section 3.2).

The modeled thermal stratification displayed lower values than in the observations (**Fig.6c**), particularly in the southern part of the bay (station 14, see **Fig.1b**) and nearshore, north-west off the river mouth (station 1) in a region of strong topographic variability (**Fig.1b**).

The density stratification mirrors the thermal stratification, with lower values in the model (**Fig.6d**). The stratification bias was particularly strong in the north west (stations 1,2,4), possibly due to the stratifying effect of the river discharge, which was not represented in this simulation (see Table 1). In contrast, the model stratification is in good agreement with the observed one for large depth range (>20 m). The mean stratification bias, computed over all the stations (**Table 2**), is negative (-5.6 10^{-2} σ m^{-1}) over the entire region. Note that the bias stratification is almost three times weaker in the bay (-1.46 σ m^{-1}) than north of the bay (-4.15 σ m^{-1}).

At P1, the model SST fluctuated between 17.5°C and 23°C over the summer period (**Fig. 7a**). The lowest temperatures encountered in early January coincided approximately with two wind intensifications (**Fig. 7.d)**, whereas the highest temperatures were found in early March coinciding with a wind relaxation. Correlation between SST and wind stress was ~ -0.5 (with SST lagging wind stress by one day). The model SST was lower than the observed climatological temperature over January-February, but within the range of observed SST variability. Bottom temperature fluctuated between ~16°C and ~18°C, roughly in phase with SST but with a weaker amplitude (**Fig.7b**). The model bottom temperature tended to exhibit a warm bias, but remained within the range of observed variability. Due to these biases, the summer-average thermal stratification was weaker in the model (~0.16 °C m^{-1}; **Fig.7c**) than in the observations (~0.25 °C m^{-1}; **Table 3**).

c. Impact of the wind diurnal cycle

The wind diurnal cycle was introduced in simulation D03-B (see section 2.5.a; **Table 1**). To examine its effect on the thermal stratification we first compare the modeled temperature diurnal cycle to measurements at P2, a shallow station in the bay (see **Fig.1b**) where hourly measurements were collected during January-March 2013. The observed ~2m depth temperature varied between 16.7°C at 3:00-4:00 and ~17.7°C at 15:00, while the bottom temperature was minimum (~15.7°C) at ~9:00 and maximum (~ 16.2°C) at ~ 14:00-15:00. The observed maximum (respectively minimum) of temperature difference (between surface and bottom layers) was ~1.5ºC (respectively ~1°C) at ~15:00 (respectively 0:00-6:00; **Fig.5b**). The daily-average observed stratification at P2 was 0.42 σ m^{-1} (using a constant salinity of 35 psu, as no salinity measurements were collected at P2).

Both D03-A and DO3-B 2m depth temperature at P2 were ~2°C warmer than the observed. The D03-B temperature maximum increased slightly (<0.5°C) with respect to that in D03-A due to the inclusion of the wind diurnal cycle. It was reached at ~18-19:00, ~1 hour earlier than in D03-A (**Fig.8a**). The modeled near-bottom temperatures were very similar (**Fig.8b**). The maximum thermal stratification reached 0.5ºC m^{-1} (respectively 0.4°C m^{-1}) near 18:00 (respectively 19:00) in D03-B (respectively D03-A) (**Fig.8c**). This contrasts with the stronger stratification (~0.8°C m^{-1}) and timing (~15:00) of the observed maximum thermal stratification at P2 (**Fig.5b**). Thus the wind diurnal cycle seemed to have only a weak impact on the diurnal variations of the subsurface stratification at P2. However, modeled vertical gradients of temperature in the surface layer can be relatively large (up to ~ 1°C/m, see **Fig.S7**). Consequently, the effect on the averaged surface-bottom density stratification north of the bay (at P1) was larger, resulting in a stratification increase of 19% over the whole summer (**Table 3**).

d. Impact of chlorophyll-induced shortwave heat absorption

The introduction of the effect of chlorophyll-related turbidity on shortwave absorption in the water column (see section 2.5.b) in D03-C had a significant impact on the thermal stratification: while the surface temperature was occasionally slightly increased (*e.g.*~0.5-1°C in late January; **Fig.9a**), the bottom temperature was decreased by ~0.5-1°C over the entire summer with respect to D03-B (**Fig.9b**), resulting in a thermal stratification increase of 0.05-0.1°C m^{-1}. On average, the density stratification at P1 reached 5.9 10^{-2} σ m^{-1}, i.e. a 20% increase with respect to D03-B (**Table 3**). The stratification computed at stations located in the bay was also improved (**Table 2**).

e. Impact of the tidal forcing

Paracas bay is microtidal, with sea level variations between ~ +/-0.2 m north of the bay at Pisco harbour. The model reproduced well the tidal sea level variations north of the bay (Pisco station; **Fig.S6**). The modeled tidal currents were weak (~less than 5 cm s^{-1}, figure not shown). Overall, the impact of the tidal forcing on the stratification at P1 and other stations was negligible.

f. Impact of the wind correction

The WRF wind correction (see section 2.4b) had the strongest impact on the stratification. The D03-E SST at P1 increased occasionally by up to 3-4°C with respect to D03-B (*e.g.* in February, **Fig.9d**). D03-E bottom waters were also ~0.5°C warmer (**Fig.9e**). The thermal stratification change with respect to D03-B was moderate (< 0.05°C m^{-1}) in early January and late March, but stronger (up to ~0.15°C m^{-1}) in February (**Fig.9f**), due to the stronger wind correction during this month (Figure not shown). The SST and bottom temperature increase in D03-E likely resulted from both a wind-driven upwelling of shallower and warmer waters into the bay and a reduction of wind-driven mixing, which overcompensated the increased latent heat loss at P1 (+70% increase in D03-E with respect to D03-B). Note that a comprehensive heat budget of the surface mixed layer (which is beyond the purpose of this work) would be needed to evaluate precisely the contribution of the respective mechanisms (advection, vertical mixing, air-sea exchanges) at stake. Overall, the average stratification increase at P1 due to the wind correction was 44% (**Table 3**). Stratification bias was also greatly reduced at all stations, especially in the bay (**Table 2**).

g. Impact of the river discharge

A strong Pisco river discharge in summer (**Fig.S7**) may enhance the density stratification in the bay by decreasing the near-surface salinity. Taking into account the discharge seasonal cycle in the model in D03-G, the summer-mean modeled surface salinity was lower near the river mouth than in the bay (**Fig.10a**). However, the modeled salinity was ~1-2 psu higher than the observed near the coast north of the bay. During wind relaxations, the river plume was oriented towards the bay (**Fig.10b**) and salinity at P1 decreased by more than 1 psu (*e.g.* mid January) and 3 psu (*e.g.* early March) (**Fig. 11).** Over the entire summer period, the average density stratification at P1 increased by 10% due to river runoff (**Table 3**).

3.3 Circulation in the bay

The modeled circulation in Paracas Bay is examined in this section. Simulation D03-I which includes the main forcings and parameterizations impacting the stratification (see **Table 1**) is analyzed. Note that the circulation patterns described in the following subsections are nearly unchanged in the other modelling experiments (i.e D03-A, D03-B, etc).

a. Mean circulation and stratification

The modeled surface circulation was northward in the bay and along the eastern coast, while the flow veered to the northwest and intensifies north of the Paracas peninsula (**Fig.12a**). Surface velocities were ~10 cm s^{-1} in the bay, reaching 20 cm s^{-1} near the western coast of the bay, consistently with the wind intensification north of the peninsula (not shown). In the bottom layer, offshore cold water flowed into the bay along its western side, and then southward in the bay, with velocities around ~1 cm s^{-1} (**Fig.12b**). At the entrance of the bay, the northward surface flow was concentrated in a shallow, 2 to 3-m-thick surface layer, and intensified along the western side of the bay mouth (**Fig.12c**).

b. Circulation and stratification under strong wind

The circulation and stratification during the windiest day in March (see red star in **Fig.7d**) were examined (**Figs.12d-f**). The patterns were nearly similar to the summer averages. The surface circulation was intensified, with velocities up to 12-15 cm s^{-1} in the bay (**Fig.12d**). A weaker (~ 5-10 cm s^{-1}) northward circulation took place in the south-western sector of the bay. In the bottom layer (**Fig.12e**), the southward velocity reached 2.5 cm s^{-1} near the eastern side of the bay mouth and it was reduced (~ 1 cm s^{-1}) within the bay except in the south-eastern sector (~ 1.5-2 cm s^{-1}). At the bay mouth (**Fig.12f**), the thermal stratification was reduced with respect to mean conditions due to enhanced wind-driven vertical mixing in the surface layer and to enhanced friction in the bottom layer (not shown). Other strong wind events were investigated and showed qualitatively similar patterns (see **Fig.S9**).

c. Circulation and stratification under weak wind

The circulation and stratification during the least windy day of the period (early March, see blue star in **Fig.7d**) were examined (**Figs.12g-i**). Near the bay mouth, the southward surface flow associated to a shoaling and penetration over the shelf of the PCUC splitted into a westward branch (~8 cm s^{-1}) and a weak southward branch (~4 cm s^{-1}) entering the bay. The southward flow drove a sluggish (<5 cm s^{-1}) cyclonic gyre in the bay (**Fig.12g**). In the bottom layer, the circulation was predominantly northward. It was particularly sluggish north of the bay and along the eastern shore of the bay (**Fig.12h**), suggesting a low subsurface ventilation during weak wind periods. At the bay mouth, the stratification was well marked between the surface and 6m depth (**Fig.12i**). Offshore waters entered the bay along the eastern side in a ~6 m thick surface layer, while subsurface waters exited the bay along the western side of the bay. Other weak wind events were also examined and showed qualitatively similar patterns (see **Fig.S10**). In conclusion, there was a great contrast between the circulation patterns during strong and weak winds conditions.

4. Discussion

4.1 Effects on the stratification in the bay

The impact of various physical forcings and parameterizations on the summer stratification in Paracas bay was investigated in a modelling regional framework. In the base case simulation, forced by daily winds and clear water conditions (i.e. Jerlov water type 1, see section 2.5b), the model SST was slightly lower than the observations in and north of the bay, while the bottom water was slightly warmer. Overall, the modeled density stratification was ~35% lower in the model than in the observations (at P1, near the bay mouth).

The surface cold bias in the bay was partly due to an overly strong upwelling and wind-driven mixing in the base case. Indeed, the too strong WRF winds north of the bay near Pisco airport (**Fig. 2d**) are likely to be also overestimated within the bay. Furthermore, while adding diurnal wind variations had a moderate impact (*i.e.* ~19% increase, **Table 3**) on the density stratification at P1, reducing the wind intensity over the whole model domain (see section 2.4b) resulted in a more realistic upwelling offshore and north of the Paracas peninsula and in a 44% increase of the stratification. These results highlight the high sensitivity of the model stratification to the wind forcing offshore and in the bay area. This is consistent with results from a modelling study of the Maryland lagoon shallow bays where the accuracy of the wind forcing plays a major role (*e.g.* Kang and Xia, 2022). This calls for the need (i) to use more realistic wind forcing products (*e.g.* WRF winds at sub-kilometric spatial resolution) and (ii) to routinely measure *in situ* atmospheric parameters in the bay area (see *e.g.* Niu et al., 2015, around lake Erié). Merging of model and observed surface winds (*e.g.* Kang and Kia, 2020) to produce optimal wind forcing is also an interesting perspective for future work.

The second strongest impact on the stratification was the use of a chlorophyll-related shortwave absorption in the water column. While optical properties for solar attenuation have a strong effect on upper ocean thermal conditions (and can, for example, subsequently impact hurricanes; e.g. Liu et al. 2021), their role has often been neglected in physical models of upwelling bays. Echevin et al. (2021) showed that the chlorophyll-shading effect could enhance the nearshore cold bias commonly found in EBUS models, due to the cooling of upwelled source waters associated with the chlorophyll shading. In contrast, the effect was opposite in the present study as the chlorophyll-shading induced a slight warming of the surface layer and a cooling of the subsurface layer at P1 (**Figs.9a,b**), increasing density stratification by 20% (**Table 3**). Note that this effect was parameterized in a simple manner. First, a relationship between surface chlorophyll measured by satellite and water type was used and the water type was unchanged in the vertical over the water column. Secondly, the relatively low resolution (9 km) satellite product did not represent surface chlorophyll in Paracas bay. The chlorophyll and water type values used in the bay were obtained by extrapolation of offshore values, which may lead to a temperature bias in the bay. Thirdly, the shortwave absorption profiles depending on the water type were kept constant for each month. In this respect, an interesting perspective would be to use a coupled biogeochemical model (*e.g.* Echevin et al., 2021) in order to evaluate the impacts of the chlorophyll spatio-temporal variability on the thermal structure. Last but not least, other turbidity sources (sediments resuspension and particulate organic matter; *e.g.* Xia et al. (2010) in an estuary) affecting light propagation in shallow regions also need to be taken into account in future studies.

The river discharge forcing had a weaker effect on the bay stratification (~10% increase of the stratification north of the bay; **Table 3**) due to the intermittent southward transport of low salinity riverine waters. Although this effect was relatively weak in our simulation, it could be enhanced during periods of high discharge (**Fig.S7**; Merma-Mora et al., 2022) and weak winds. Similar stratification effects due to high river discharge after the passage of hurricanes has been encountered in shallow bays of the Maryland lagoon (Kang and Xia, 2022).

Note that when the effect of wind diurnal cycle, water type and wind correction were included (D03-I; **Table 1**), the stratification biases computed over the bay area were lowest (**Table 2**). This suggests that taking into account these forcings is absolutely necessary to represent correctly the stratification in the bay area.

4.2 Effect of the wind diurnal cycle on the SST diurnal cycle

While we found that the averaged effect of the wind diurnal cycle on the stratification was moderate (19%, **Table 3**), its impacts on the thermal structure and circulation were possibly slightly biased in our model experiments for several reasons. Firstly, the wind diurnal cycle was parameterized based on wind *in situ* data over land north of the bay. Variations of the wind direction within the bay due to the coastal orography remain unknown. Improving the accuracy of the wind forcing spatio-temporal variability at hourly time scales in the bay area would likely benefit from a dedicated modelling of the surface winds using a regional atmospheric model (e.g. the WRF model) at sub-kilometric resolution. Secondly, the P2 data used to compute the thermal diurnal variations were collected in January-March 2013, a relatively cold year (ONI=-0.4), so that they may not be representative of climatological conditions. Thirdly, diurnal variations of the ERA-interim air temperature and humidity were not taken into account, which may introduce a bias in the latent and sensible heat fluxes. Last, the model may underestimate vertical mixing in the upper layer of the water column. It would thus be interesting to investigate in more detail the impact of various mixing parameterizations and parameter options in GLS at hourly time scales, which is beyond the scope of the present work.

4.3 Circulation patterns

Tidal currents were weak in our simulations (~ 2-4 cm s^{-1}, figures not shown). Using a different modelling framework, Quispe-Sánchez (2007) found tidal currents of the same order of magnitude. Note that his model was forced by the observed tidal sea level (at Pisco) along the northern and western open boundaries, which were close (~ 1 km) to the bay mouth. Furthermore, the observed wind from a single station (Pisco airport) was used to force the circulation, leading to surface currents of 2-5 cm s^{-1}, much weaker than in our simulations (~10 cm s^{-1}, **Fig. 10**). Their model did not take into account the strong offshore upwelling-favorable winds (**Fig.2**), which play a major role in the bay dynamics by sucking the surface waters out of the western side of the bay (**Fig. 12d**).

Using a two-layer reduced gravity model, Carbonel (2013) investigated the short-term (~7 days) circulation and density structure of the bay area in response to southwesterly-westerly winds. Thermal conditions corresponded to those of fall-winter 1999 and the model was spun up from a state of rest (i.e. spatially homogeneous stratification). The simulated upwelling of relatively cold waters along the western shore of the bay contrasted with our findings, which indicate slightly cooler SST along the eastern side of the bay (**Fig.6a**). However, comparing their study with ours is difficult because of the numerous differences in the wind forcing, the initial conditions and the season/duration of the simulations.

Comparing the model circulation patterns to the sketched circulation patterns based on ADCP observations (averaged flow from 0 to 10 m depth) are also informative. Poleward surface circulation was measured during a period of weak offshore wind conditions in April 2013 (Sanchez et al., 2019), which is consistent with the simulated poleward surface flow under weak wind (**Fig.12g**). In contrast, under moderate offshore upwelling-favorable winds in March 2015, the measured surface flow was southward along the western side of the bay, whereas it was northward in our simulations under comparable wind conditions (**Fig.12a**). However, note that the modelled subsurface circulation was southward and consistent with the pathways described by Sanchez et al. (2019), suggesting that the ADCP may have measured a strongly sheared flow. Last, southward surface flow was measured along the eastern side of the bay in spite of the strong winds in July 2015. This flow may be associated with the poleward alongshore current driven by a downwelling coastal wave typical of El

Niño conditions (Figure not shown). Simulating this type of situation was precluded by the so-called climatological boundary conditions used in our modelling framework, which subdued the amplitude of remotely-forced intraseasonal coastal trapped waves. The effect of such waves on the bay circulation and stratification will be investigated in future work using realistic daily boundary conditions.

5. Conclusions and perspectives

The hydrodynamics and stratification in the shallow semi-enclosed bay of Paracas influenced by offshore coastal upwelling off central Peru were studied using a regional circulation model. The wind regime within the bay is influenced by the thermal contrast between desertic land and sea and differs from the offshore upwelling-favorable wind regime associated to the eastern flank of the large-scale South Pacific anticyclone. Due to the absence of satellite winds near the coast, surface winds from the WRF high-resolution (7km) regional atmospheric model were bias-corrected to be used as model forcing.

The impact of various types of forcings was assessed: reducing the wind intensity offshore and in the bay allowed to (i) reduce the model SST cold bias in the bay associated to a too strong vertical mixing and (ii) increase significantly the stratification in the bay; the parametrization of the shortwave flux penetration induced a cooling of the subsurface water, increasing the stratification; the diurnal cycle of the wind impacted on the stratification, but this needs to be interpreted with caution given the remaining bias in the temperature diurnal cycle phase. Freshwater discharge from the Pisco river north of the bay also increased slightly the stratification in the bay, in particular during weak wind conditions allowing the river plume to enter the bay. However, note that this effect could be underestimated given the discharge strong interannual variability. Last, the tidal forcing had no impact on the stratification and circulation, generating currents much weaker than wind-driven currents.

The summer circulation, characterized for the first time using a model, is mainly forced by the wind variability: under strong wind conditions it is driven by the wind-forced upwelling, with northward surface currents transporting the bay warm surface waters outward and subsurface currents transporting cold subsurface waters into the bay along its western shore. In contrast, under weak wind conditions, a surface southward current over the inner shelf transported warm shelf waters into the bay, generating a cyclonic circulation in the bay. The subsurface waters flowed along the western shore before exiting the bay. The modelled circulation patterns were not in contradiction with those sketched from short term oceanographic cruises. However, a description of the circulation in Paracas bay based on long-term current measurements is still lacking.

Several perspectives can be drawn from this work. Firstly, using a more accurate wind forcing is key to improve the realism of the simulation. Secondly, a higher horizontal resolution of the ocean model in the bay (e.g. < 100 m) would provide more detailed circulation patterns. Thirdly, intraseasonal coastal waves propagating poleward along the coast and having a strong influence on the alongshore flow on the Peruvian shelf (*e.g.* Colas et al., 2008 during El Niño conditions) may occasionally force a flux of relatively warm surface waters from the inner shelf north of the bay into the bay. This forcing needs to be taken into account in future modelling experiments. Lagrangian diagnostics will be useful to determine more accurately the exchanges between the bay and the outer shelf and the residence time in the bay (a relevant information for various ecological questions). Last, our hydrodynamical model also needs to be coupled with a biogeochemical model simulating the oxygen cycle (*e.g.* the PISCES model previously used in the Peruvian upwelling system, *e.g.* Espinoza-Morriberon et al., 2021) to study the drivers of hypoxic and anoxic events in the bay (Merma-Mora et al., 2022) and provide guidance for a sustainable management of aquaculture. This challenging task will likely require coupling with a diagenetic model to take into account the sediment oxygen demand (*e.g.* Capet et al., 2013).

Acknowledgements

The numerical simulations were performed on the IDRIS ADA and Jean-Zay high performance computers under DARI projects A0070101140 and A0090101140. GLORYS global ocean model outputs were provided by the Copernicus Marine Environment Monitoring Service (CMEMS). C. Arellano was funded by National council for science, technology and technological innovation (CONCYTEC), PROCIENCIA Grant N° E032-2016-01 FONDECYT “Becas de Doctorado en el Extranjero”, the Peruvian Sea Institute (IMARPE) and Institute de Recherche pour le Développement (IRD). V. Echevin and F. Colas are funded by IRD. We would like to thank the Research Institute of the Peruvian Sea (IMARPE), especially the staff of the Coastal Laboratory of Pisco, as well as the National Water Authority (ANA), the National Service of Meteorology and Hydrology of Peru (SENAMHI) and the PLUSPETROL and Environmental Resources Management (ERM) companies for providing the monitoring data. This work is a contribution to the cooperative agreement between IMARPE and the Institute de Recherche pour le Developpement (IRD) through the LMI DISCOH, JEAI DYSRUP and GDRI DEXICOTROP projects.

References

Aguirre-Velarde, A., Thouzeau, G., Jean, F., Mendo, J., Cueto-Vega, R., Kawazo-Delgado, M., Vásquez-Spencer, J., Herrera-Sanchez, D., Vega-Espinoza, A., and Flye-Sainte-Marie, J., 2019. Chronic and severe hypoxic conditions in Paracas Bay, Pisco, Peru: Consequences on scallop growth, reproduction, and survival. Aquaculture, 512(February):734259.

Arntz, W. E., Tarazona, J., Gallardo, V. A., Flores, L. A., & Salzwedel, H., 1991. Benthos communities in oxygen deficient shelf and upper slope areas of the Peruvian and Chilean Pacific coast, and changes caused by El Niño. Geological Society, 58, 131–154.

Astudillo, O., Dewitte, B., Mallet, M., Frappart, F., Rutllant, J. A., Ramos, M., and Bravo, L., 2017. Remote Sensing of Environment Surface winds off Peru-Chile : Observing closer to the coast from radar altimetry. Remote Sensing of Environment, 191:179–196.

Barber, R. T., and Chavez, F. P., 1983. Biological consequences of El Niño, Science, 222, 1203–1210, doi:10.1126/science.222.4629.1203.

Bentamy, A., and Fillon, D. C., 2012. Gridded surface wind fields from Metop/ASCAT measurements. Int. J. Remote Sens. 33, 1729–1754. doi: 10.1080/01431161.2011.600348.

Bernie, D. J., Woolnough, S. J., Slingo, J. M., & Guilyardi, E., 2005. Modeling Diurnal and Intraseasonal Variability of the Ocean Mixed Layer, *Journal of Climate*, *18*(8), 1190-1202. Retrieved Feb 3, 2022, from https://journals.ametsoc.org/view/journals/clim/18/8/jcli3319.1.xml

Berrisford, P, Dee, DP, Poli, P, Brugge, R, Fielding, M, Fuentes, M, Kållberg, PW, Kobayashi, S, Uppala, S, Simmons, A., 2011. The ERA-Interim archive Version 2.0, ERA Report Series - ECMWF, from https://www.ecmwf.int/node/8174

Boé, J., Hall, A., Colas, F., McWilliams, J. C., Qu, X., Kurian, J., and Kapnick, S. B., 2011. What shapes mesoscale wind anomalies in coastal upwelling zones? Climate dynamics, 36(11):2037–2049.

Cabello, R.,J. Tam, and Jacinto, M. E., 2002. Procesos naturales y antropogenicos asociados al evento de mortalidad de conchas de abanico ocurrido e la Bahia de Paracas (Pisco, Peru) en junio del 2000, Rev. Peru. Bioi., 9,94-110.

Capet, X. J., P. Marchesiello, and J. C. McWilliams, 2004. Upwelling response to coastal wind profiles, Geophysical Research Letters, 31 , L13311, doi:10.1029/2004GL020123.

Capet, A., J.-M. Beckers, and M. Grégoire, 2013. Drivers, mechanisms and long-term variability of seasonal hypoxia on the Black Sea northwestern shelf – is there any recovery after eutrophication? Biogeosciences, 10, 3943–3962, doi:10.5194/bg-10-3943-2013

Carbonel, C. A. A., 2013. Un modelo de gravedad reducida de la hidrodinámica y termodinámica en zona costera. Caso de estudio: Bahías de Pisco y Paracas. Revista de Investigación de Física 16, 131601401.

Chacón, E., 2014. Predicción sedimentaria en base a características en el margen continental peruano mediante modelos de estadística espacial. Tesis para optar el título de Ingeniero estadístico, Universidad Nacional de Ingeniería.

Chaigneau, A., Dominguez, N., Eldin, G., Vasquez, L., Flores, R., Grados, C., and Echevin, V., 2013. Near-coastal circulation in the Northern Humboldt Current System from shipboard ADCP data. Journal of Geophysical Research: Oceans, 118:5251–5266.

Chamorro, A., Echevin, V., Dutheil, C., Tam, J., Gutiérrez, D., and Colas, F., 2021. Projection of upwelling - favorable winds in the Peruvian upwelling system under the RCP8 . 5 scenario using a high - resolution regional model. Climate Dynamics, (0123456789).

Chavez, F. P., Bertrand, A., Guevara-Carrasco, R., Soler, P., and Csirke, J., 2008. The northern Humboldt Current System: Brief history, present status and a view towards the future. Progress in Oceanography, 79(2-4):95–105.

Colas, F., X. Capet, J. C. McWilliams, and A. Shchepetkin, 2008, 1997–98 El Niño off Peru: A numerical study, Prog. Oceanogr., 79, 138–155.

Cuellar-Martinez, T., A. Huanca-Ochoa, S. Sanchez, A. Aguirre-Velarde, D. Correa, K. Egoavil Gallardo, H. Lujan-Monja, J. Ipanaque-Zapata, F. Colas, J. Tam, D. Gutierrez, 2021. Harmful blooms of Alexandrium ostenfeldii and paralytic shellfish toxins in scallops from Paracas Bay, Peru; Marine Pollution Bulletin, https://doi.org/10.1016/j.marpolbul.2021.112988.

Cueto-Vega R, Flye-Sainte-Marie J, Aguirre-Velarde A, Jean F, Gil-Kodaka P, Thouzeau G., 2021. Size-based survival of cultured Argopecten purpuratus (L, 1819) under severe hypoxia. J World Aquac Soc. 1–23. https://doi.org/10.1111/jwas.12777

Da Silva, A. M., Young, C. C., and Levitus, S., 1994. Atlas of Surface Marine Data 1994, vol. 1, ALGORITHMS and Procedures, Technical Report. Washington, D.C: U.S. Department of Commerce.

Dee, D. P., et al, 2011. The ERA-Interim reanalysis: configuration and performance of the data assimilation system. Q J R Meteorol. Soc. A 137:553–597. https://doi.org/10.1002/qj.828.

Drake, P. T., Edwards, C. A., Morgan, S. G., Satterthwaite, E.V., 2018. Shoreward swimming boosts modeled nearshore larval supply and pelagic connectivity in a coastal upwelling region. Journal of Marine Systems, 187, 96-110, https://doi.org/10.1016/j.jmarsys.2018.07.004.

Echevin, V., Albert, A., Lévy, M., Graco, M., and Aumont, O., 2014. Intraseasonal variability of nearshore productivity in the Northern Humboldt Current System: The role of coastal trapped waves. Continental Shelf Research, pages 14–30.

Echevin, V., Hauschildt, J., Colas, F., Thomsen, S., & Aumont, O., 2021. Impact of chlorophyll shading on the Peruvian upwelling system. Geophysical Research Letters, 48, e2021GL094429. https://doi.org/10.1029/2021GL094429

Egbert, G. D. and Erofeeva, S. Y., 2002. Efficient Inverse Modeling of Barotropic Ocean Tides. Journal of Atmospheric and Oceanic Technology, 19:183–204.

El Commercio, 2019. https://elcomercio.pe/_vamos/peru/paracas-balneario-de-ica-planea-recibir-un-millon-de-turistas-el-2020-fotos-noticia/?ref=ecr.

Espinoza-Morriberon, D., Echevin, V., Gutiérrez, D., Tam, J., Graco, M., Ledesma, J., and Colas, F., 2021. Evidence and drivers of ocean deoxygenation off peru over recent past decades. Scientific Reports.

Fairall, C. W., Bradley, E. F., Hare, J. E., Grachev, A. A., and Edson, J. B., 2003. Bulk parameterization of air-sea fluxes: Updates and verification for the COARE algorithm. Journal of Climate, 16(4):571–591.

Flores-Valiente, J., Tam, J., Brochier, T., Colas, F., Pecquerie, L., Aguirre-Velarde, A., Mendo, J., and Lett, C., 2019. Larval supply of Peruvian scallop to the marine reserve of Lobos de Tierra Island: A modeling approach. Journal of Sea Research, 144, 142-155. https://doi.org/10.1016/j.seares.2018.12.003

Fuenzalida, R., Schneider, W., Garcés-Vargas, J., Bravo, L., and Lange, C., 2009. Vertical and horizontal extension of the oxygen minimum zone in the eastern South Pacific Ocean. Deep-Sea Research Part II: Topical Studies in Oceanography, 56:992–1003.

Guzmán, M., Chávez, J., Morón, O., Sánchez, S., Flores, G., 1997. Evaluación de la calidad del medio ambiente marino en la bahía de Pisco-Paracas, 22 a 24 de mayo 1996.Inf. Prog. Inst. Mar Perú 54.

Hilt, M., F. Auclair, R. Benshila, L. Bordois, X. Capet, L. Debreu, F. Dumas, S. Jullien, F. Lemarié, P. Marchesiello, C. Nguyen, L. Roblou, 2020. Numerical modelling of hydraulic control, solitary waves and primary instabilities in the Strait of Gibraltar, Ocean Modelling, 151,https://doi.org/10.1016/j.ocemod.2020.101642.

Hodges, B. R., Imberger, J., Saggio, A., & Winters, K. B., 2000. Modeling basin-scale internal waves in a stratified lake. *Limnology and oceanography*, *45*(7), 1603-1620.

Jackett, D. R. and T. J. McDougall, 1995. Minimal Adjustment of Hydrostatic Profiles to Achieve Static Stability, Journ of Atmos. and Oceanic Techn., vol. 12, pp. 381-389.

Jerlov, N., G., 1976. Marine Optics. Number 45–59. Elsevier; New York.

Jin, X., and Weller, R. A., 2008. Multidecade global flux datasets from the objectively analyzed air-sea fluxes (oaflux) project: Latent and sensible heat fluxes, ocean evaporation, and related surface meteorological variables. *OAFlux Project Tech. Rep. OA-2008-01*, *74*.

Kahru, M., Mitchell, B., Diaz, A., and Miura, M., 2004. MODIS detects a devastating algal bloom in Paracas Bay, Peru. Eos Trans. AGU, 85:465 – 72.

Kang, X., & Xia, M., 2020. The study of the hurricane-induced storm surge and bay-ocean exchange using a nesting model, Estuaries and Coasts, 43, 1610-1624, https://doi.org/10.1007/s12237-020-00695-3.

Kang, X., & Xia, M., 2022. Stratification variability in a lagoon system in response to a passing storm, Limnology and Oceanography, 67, 511-521. https://doi.org/10.1002/lno.12016.

Kumar, B. P., Vialard, J., Lengaigne, M., Murty, V. S. N., and Mcphaden, M. J., 2012. TropFlux : air-sea fluxes for the global tropical oceans - description and evaluation. Clim Dyn, 38:1521–1543.

Merma, L., Colas, F., Cardich, J., Sánchez, S., Flores, E., Lorenzo, A., Aguirre-Velarde, A., Correa, D., Gutiérrez D., 2022. Bottom-water hypoxia in Paracas Bay (Peru, 13.8ºS) associated to seasonal and synoptic time scale variability of winds and water stratification. Submitted to Estuarine, Coastal and Shelf Science.

Lagos, N.A., Benítez, S., Duarte, C., Lardies, M.A., Broitman, B.R., Tapia, C., Tapia, P., Widdicombe, S., Vargas, C.A., 2016. Effects of temperature and ocean acidification on shell characteristics of Argopecten purpuratus: implications for scallop aquaculture in an upwelling-influenced area. Aquac. Environ. Interact. 8:357–70.doi: 10.3354/aei00183

Lavik, G., Stuhrmann, T., Bruchert, V., Van der Plas, A., Mohrholz, V., et al., 2008. Detoxification of sulphidic African shelf waters by blooming chemolithotrophs. Nature, 457 (7229), 581–584.

Lellouche, J.-M., Galloudec, Le, O., Drévillon, M., Régnier, C., Greiner, E., Garric, G., Ferry, N., Desportes, C., Testut, C. E., Bricaud, C., Bourdallé-Badie, R., Tranchant, B., Benkiran, M., Drillet, Y., Daudin, A., and De Nicola, C., 2013. Evaluation of real time and future global monitoring and forecasting systems at Mercator Océan. Ocean Sci. Discuss. 9, 1123–1185. doi: 10.5194/osd-9-1123-2012.

Liu, Y., He, R. and Lee, Z., 2021. Effects of Ocean Optical Properties and Solar Attenuation on the Northwestern Atlantic Ocean Heat Content and Hurricane Intensity. Geophysical Research Letters, 48(13), p.e2021GL094171.

Mason, E., Molemaker, J., Shchepetkin, A. F., Colas, F., Mcwilliams, J. C., and Sangrà, P., 2010. Procedures for offline grid nesting in regional ocean models. Ocean Modelling, 35(1-2):1–15.

Montes, I., Colas, F., Capet, X., and Schneider, W., 2010. On the pathways of the equatorial subsurface currents in the eastern equatorial Pacific and their contributions to the Peru-Chile Undercurrent. Journal of Geophysical Research: Oceans, 115(9):1–16.

Niu, Q., Xia, M., Rutherford, E. S., Mason, D. M., Anderson, E. J., and Schwab, D. J., 2015. Investigation of interbasin exchange and interannual variability in Lake Erie using an unstructured-grid hydrodynamic model, J. Geophys. Res. Oceans,120,2212–2232, doi:10.1002/2014JC010457.

Ohde, T., 2018. Coastal sulfur plumes off Peru during El Niño, La Niña, and neutral phases. Geophys. Res. Letters, 45, 7075–7083. https://doi.org/10.1029/2018GL077618

O´Reilly, J.E., S. Maritorena, B. G. Mitchell, D. A. Siegel, K. L. Carder, S. A. Garver, M. Kharu and C. McClain, 1998. Ocean color chlorophyll algorithms for SeaWIFS, J. Geophys. Res., 103, C11, 24,937-24,953, doi:10.1029/98JC02160.

Paulmier, A., and D. Ruiz-Pino, 2008. Oxygen minimum zones (OMZs) in the modern ocean. Progress in Oceanography, 80, 364, 113-128. https://doi.org/10.1016/j.pocean.2008.08.001

Paulson, C. A. and Simpson, J. J., 1977. Irradiance Measurements in the Upper Ocean. Journal of Physical Oceanography, 7 (952-956).

Pawlowicz, R., Beardsley, B., and Lentz, S., 2002. Classical tidal harmonic analysis including error estimates in MATLAB using TDE. Computers and Geosciences, 28(8):929–937.

Penven, P., Roy, C., Colin de Verdière, A., Largier, J., 2000. Simulation of a coastal jet retention process using a barotropic model, Oceanologica Acta, 23, 5, 615-634.https://doi.org/10.1016/S0399-1784(00)01106-3.

Penven, P., Marchesiello, P., Debreu, L., and Lefévre, J., 2008. Software tools for pre- and post-processing of oceanic regional simulations. Environ. Model. Softw. 23, 660–662. doi: 10.1016/j.envsoft.2007.07.004

Pitcher, G.C., Aguirre-Velarde, A., Breitburg, D., Cardich, J., Carstensen, J., Conley, D.J., Dewitte, B., Engel, A., Espinoza-Morriberón, D., Flores, G., Garçon, V., Graco, M., Grégoire, M., Gutiérrez, D., Martin Hernandez-Ayon, J., May Huang, H-H., Isensee, K., Elena Jacinto, M., Levin, L., Lorenzo, A., Machu, E., Merma, L., Montes, I., SWA, N., Paulmier, A., Roman, M., Rose, K., Hood, R., Rabalais, N.N., Gro V. Salvanves, A., Salvatteci, R., Sánchez, S., Sifeddine, A., Wahab Tall, A., van der Plas, A.K., Yasuhara, M., Zhang, J., Zhu, Z., 2021. System controls of coastal and open ocean oxygen depletion, Progress in Oceanography, doi: https://doi.org/10.1016/j.pocean.2021.102613.

Quispe-Sánchez, J., 2007. Simulación de la hidrodinámica en la Bahía de Paracas, Pisco-Perú; utilizando forzantes físicos. Master's thesis Universidad Nacional Mayor de San Marcos. http://cybertesis.unmsm.edu.pe/handle/20.500.12672/2537

Renault, L., Hall, A., and Mcwilliams, J. C., 2016. Orographic shaping of US West Coast wind profiles during the upwelling season. Climate Dynamics, pages 273–289.

Rodríguez, E., Morris, C. S., Belz, J. E., Chapin, E. C., Martin, J. M., Daffer, W., and Hensley, S., 2005. An Assessment of the SRTM Topographic Products. Technical report, Jet Propulsion Laboratory, Pasadena, California.

Sanchez, S., Jacobo, N., Bernales, A., Franco, A., Quispe, J., and Flores G., 2019. Seasonal Variability in the Distribution of Phytoplankton in Paracas Bay/Peru, as a Response to Environmental Conditions. Journal of Environmental Science and Engineering B 8, 7-16. doi:10.17265/2162-5263/2019.01.002

Shchepetkin, A. F. and McWilliams, J. C., 2005. The regional oceanic modeling system (ROMS): A split-explicit, free-surface, topography-following-coordinate oceanic model. Ocean Modelling, 9(4):347–404.

Shchepetkin, Alexander F., and James C. McWilliams. "Correction and commentary for “Ocean forecasting in terrain-following coordinates: Formulation and skill assessment of the regional ocean modeling system” by Haidvogel et al., J. Comp. Phys. 227, pp. 3595–3624." *Journal of Computational Physics* 228.24 (2009): 8985-9000.

Schunck, H., Lavik, G., Desai, D. K., Großkopf, T., Kalvelage, T., Contreras, S., Siegel, H., Holtappels, M., Lo, C. R., Rosenstiel, P., Schilhabel, M. B., Graco, M., Schmitz, R. A., Kuypers, M. M. M., and Laroche, J., 2013. Giant Hydrogen Sulfide Plume in the Oxygen Minimum Zone off Peru Supports Chemolithoautotrophy. PloS one, 8(8).

Skamarock, W, Klemp J., 2008. A time-split nonhydrostatic atmospheric model for weather research and forecasting applications. J Comp Phys 227:3465–3485. https://doi.org/10.1016/j.jcp.2007.01.037

Taylor, M.H., Wolff, M., Mendo, J., Yamashiro, C., 2008. Changes in trophic flow structure of Independence Bay (Peru) over an ENSO cycle. Progress in Oceanography 79(2–4): 336–351.

Valle-Levinson, A., Atkinson, L. P., Figueroa, D., Castro, L., 2003. Flow induced by upwelling winds in an equatorward facing bay: Gulf of Arauco, Chile. J Geophys. Res. 108:3054

Xia, M., Craig, P.M., Schaeffer, B., Stoddard, A., Liu, Z., Peng, M., Zhang, H., Wallen, C.M., Bailey, N., Mandrup-Poulsen, J., 2010. Influence of physical forcing on bottom-water dissolved oxygen within Caloosahatchee River Estuary, Florida, Journal of Environmental Engineering, 136(10), 1032-1044.

Figures

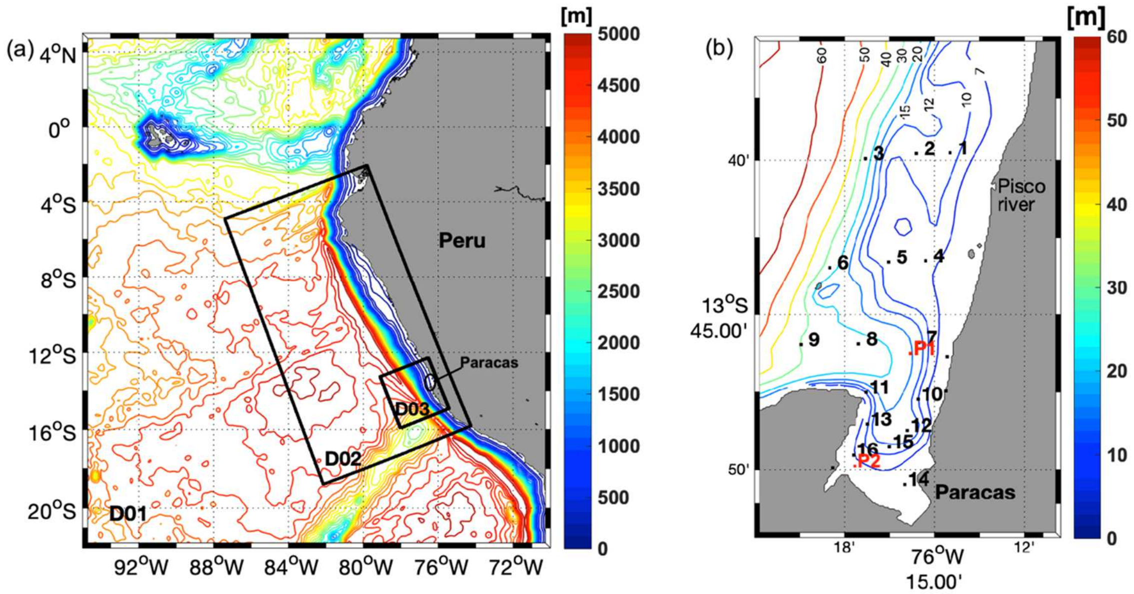

Figure 1: a) Bathymetry of D01 model grid (colored lines, in meters). D02 and D03 model domains are marked by black rectangles. b) Bathymetry of D03 model grid (colored lines, in meters). The positions of the temperature and salinity stations sampled by IMARPE-Pisco laboratory are indicated in black. P1 and P2 moorings are shown in red.

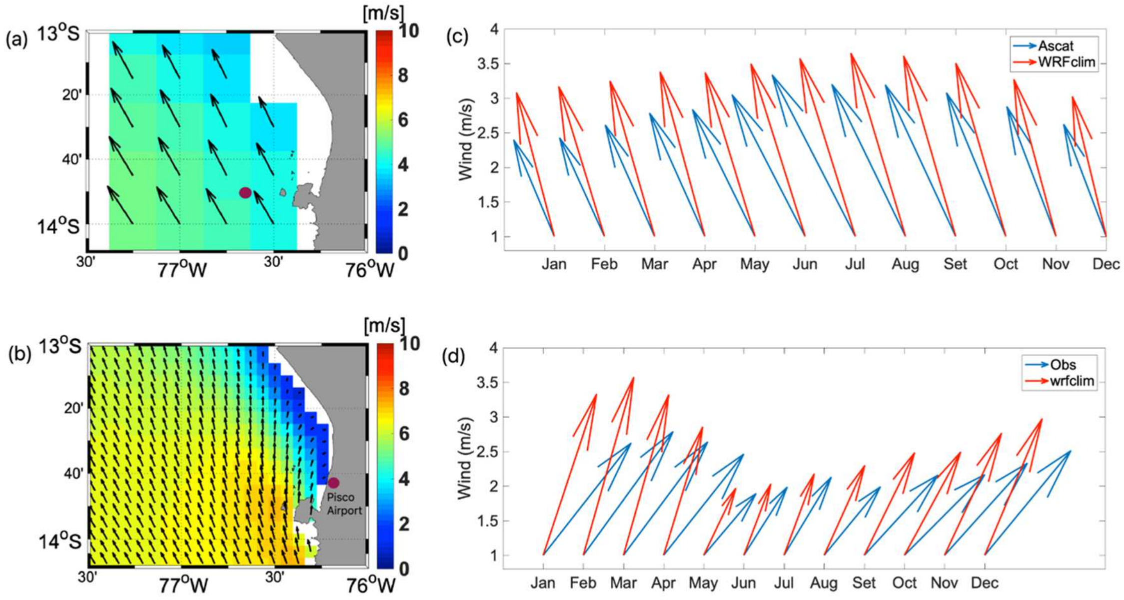

Figure 2: Summer (January-March) average of a) ASCAT and b) WRF (7km resolution) surface wind intensity (shading, in m s^{-1}) and direction (arrows). (c) ASCAT (blue arrows) and WRF (red arrows) winds west of Paracas peninsula (77ºW,13.74ºS, see red point in (a)), (d) METAR (8 m above ground, from Pisco Airport, blue arrows) and WRF surface winds (red arrows) at the coast north of the bay (see red point in (b)) .

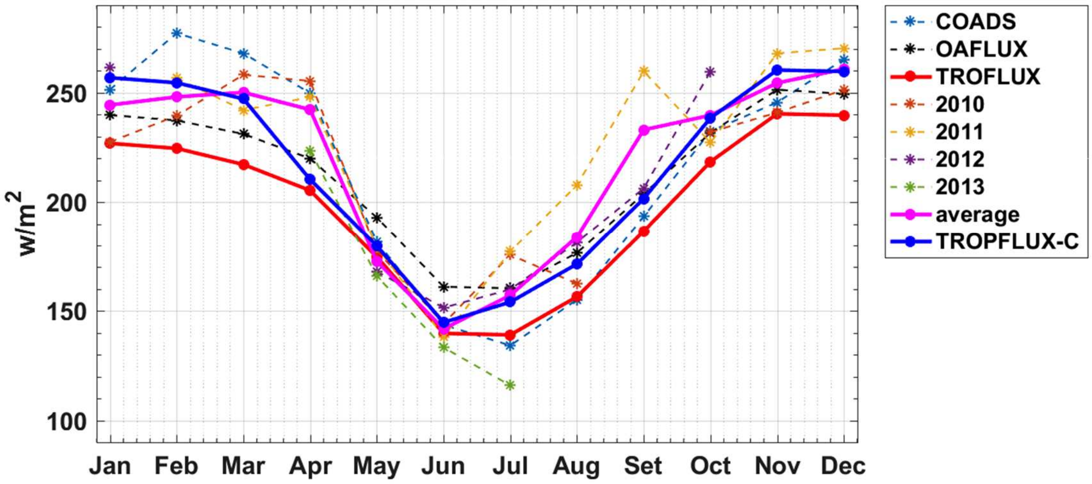

Figure 3: Climatological monthly net downward shortwave flux (in W m^{-2}) from Pisco coastal station (Sutron, magenta full line), TROPFLUX climatology (red line), TROPFLUX bias-corrected climatology (blue line). The dashed lines indicate the observed flux for different years used to compute the climatology. COADS and OAFLUX climatologies are also shown.

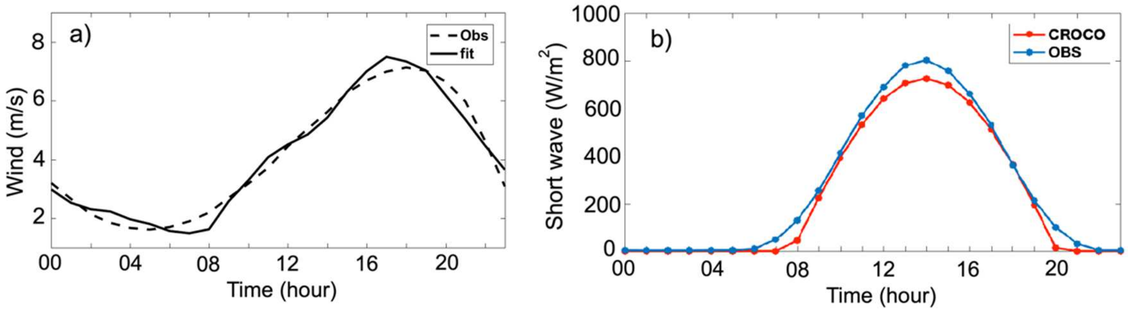

Figure 4 :(a) Observed (at Pisco Airport, dashed line) and parameterized (using a polynomial fit, full line) wind speed diurnal cycle (in m s^{-1}). (b) Observed (blue line) and parameterized (red line) downward shortwave heat flux diurnal cycle.

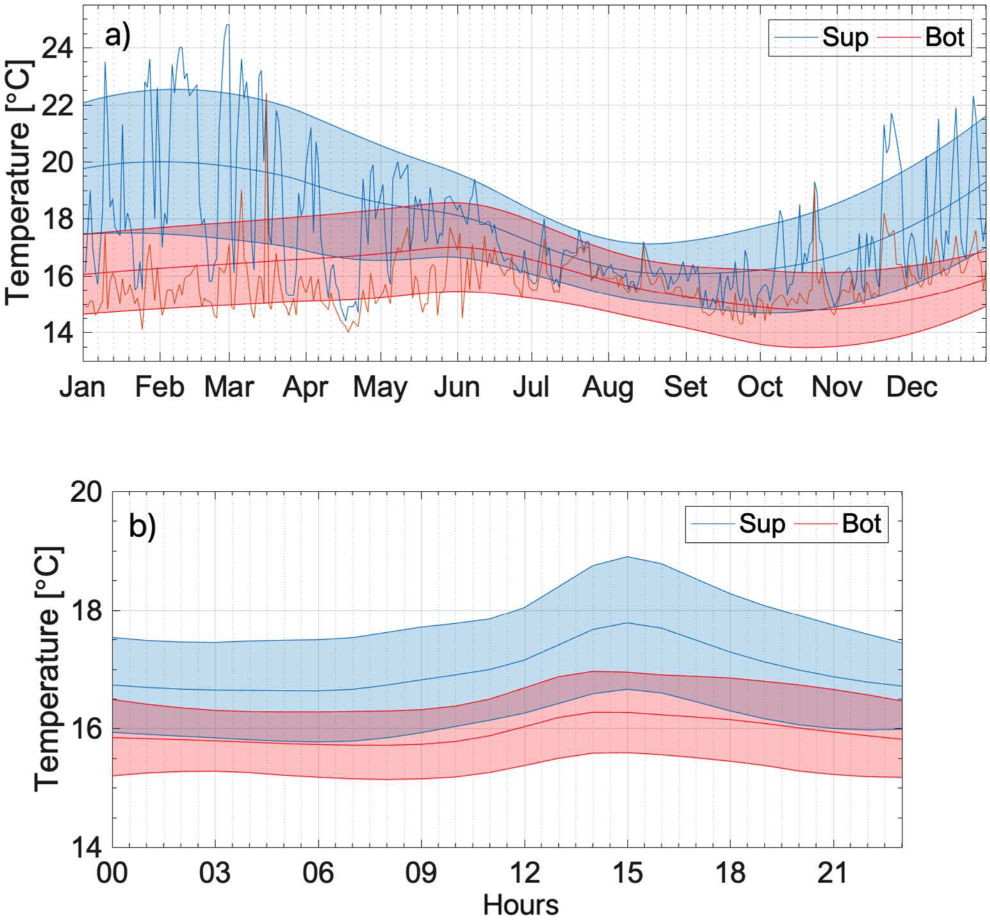

Figure 5: (a) Monthly climatology of the observed surface (1 m depth, blue line) and bottom (15 m depth, red line) temperatures at P1 station for the period 2006-2015. The lines represent the high frequency variability during 2006. (b) Composite diurnal cycle for the ~2 m depth (blue line) and bottom (~4 m depth, red line) temperatures at P2 (see Fig.1b), computed over the period January-March 2013. The shaded envelopes indicate the standard deviation of each time series.

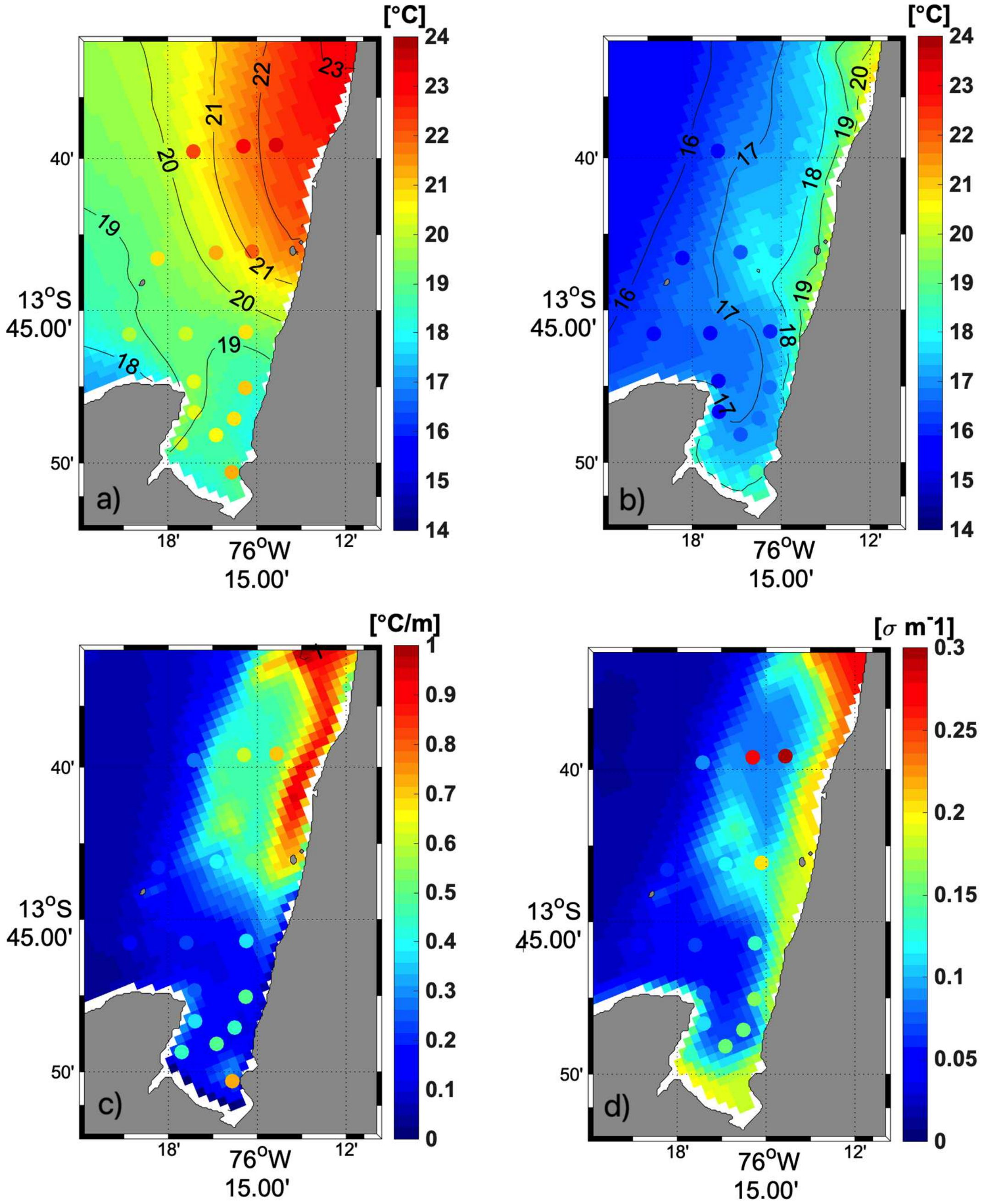

Figure 6: Summer-mean (a) SST (in °C, shading) from the model base case simulation (D03-A) and from IMARPE-Pisco laboratory stations (colored circles). (b) same as (a) for bottom temperature, (c) for thermal stratification (surface minus bottom, in °C m^{-1}) and (d) for density stratification (in σ m^{-1}).

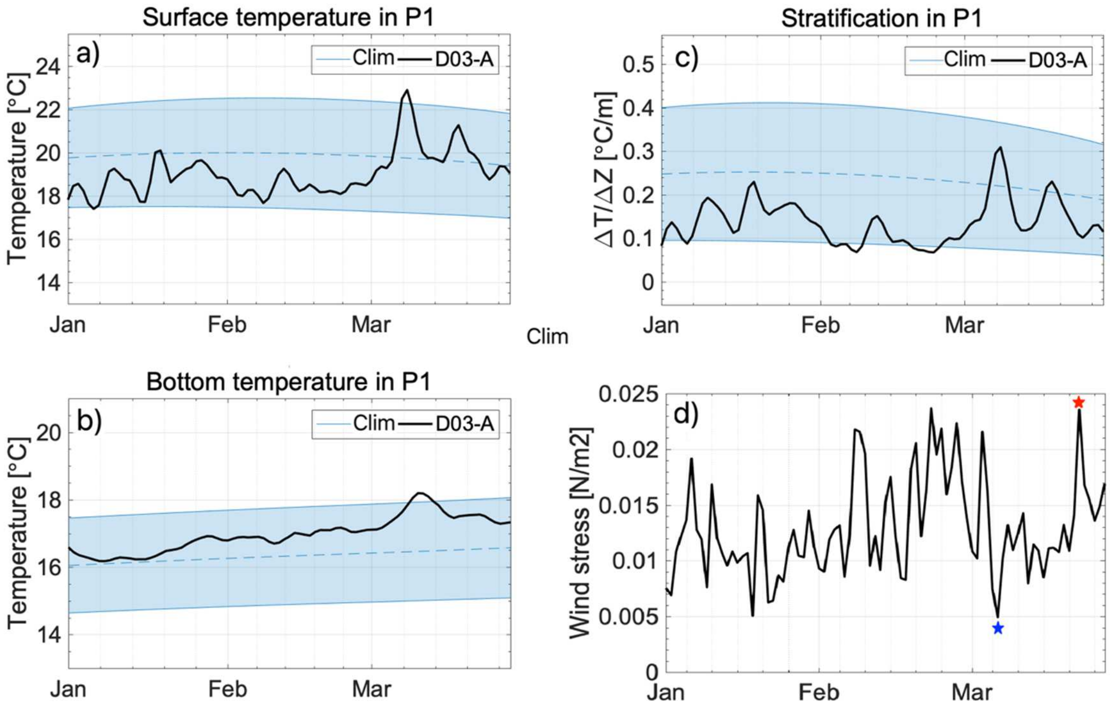

Figure 7:Time series of (a) surface, (b) bottom and (c) thermal stratification (in °C m^{-1}) at P1. The base case D03-A simulation is marked by black lines. The blue dashed line and envelope mark the observed climatology and observed standard deviation for each variable. (d) Wind stress intensity (in N m^{-2}) from D03-A at P1. The red and blue stars indicate episodes of strong and weak winds, respectively.

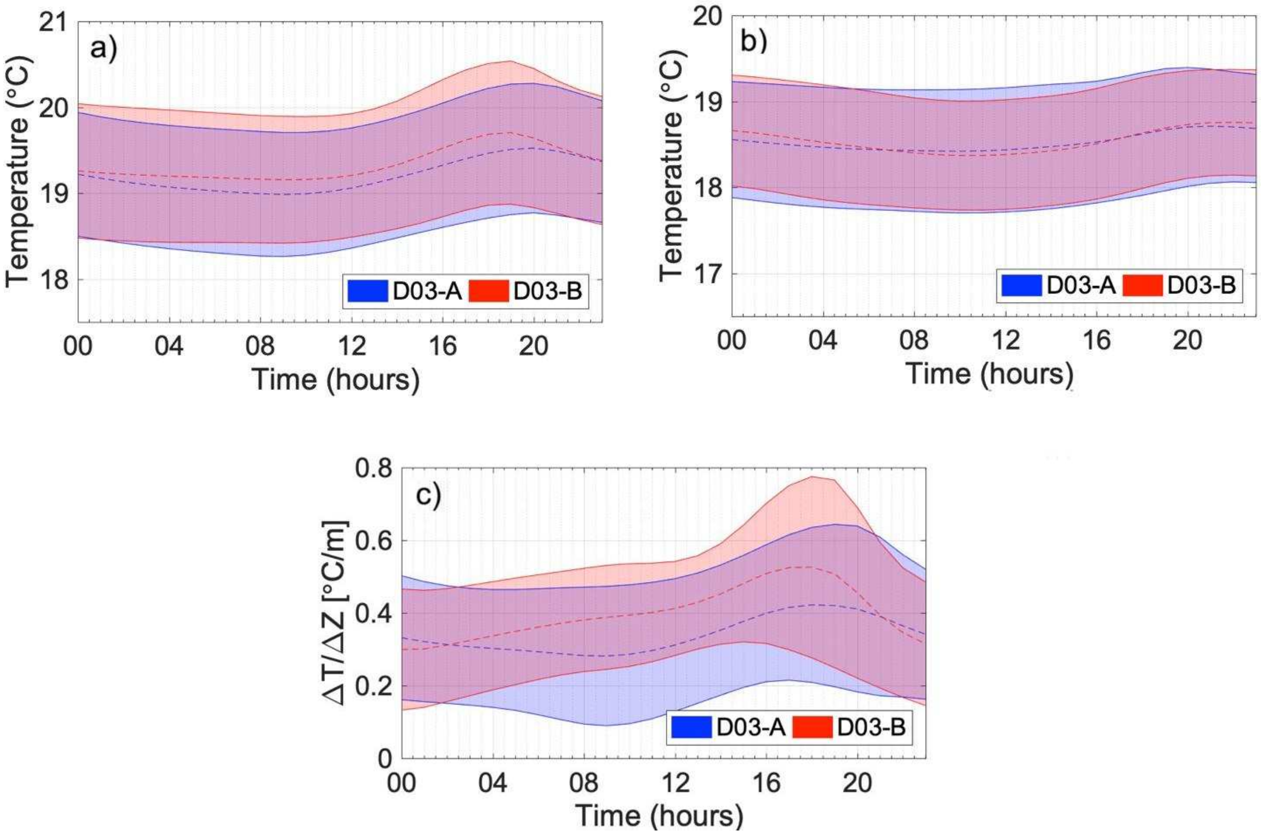

Figure 8: (a) 2m-depth, (b) 4m-depth and (c) thermal stratification (in °C m^{-1}) diurnal cycle at P2 (see Fig.1b). The colored lines and shaded envelopes represent the mean and standard deviation of simulations D03-A (blue line and shading, without wind diurnal cycle) and D03-B (red line and shading, with wind diurnal cycle).

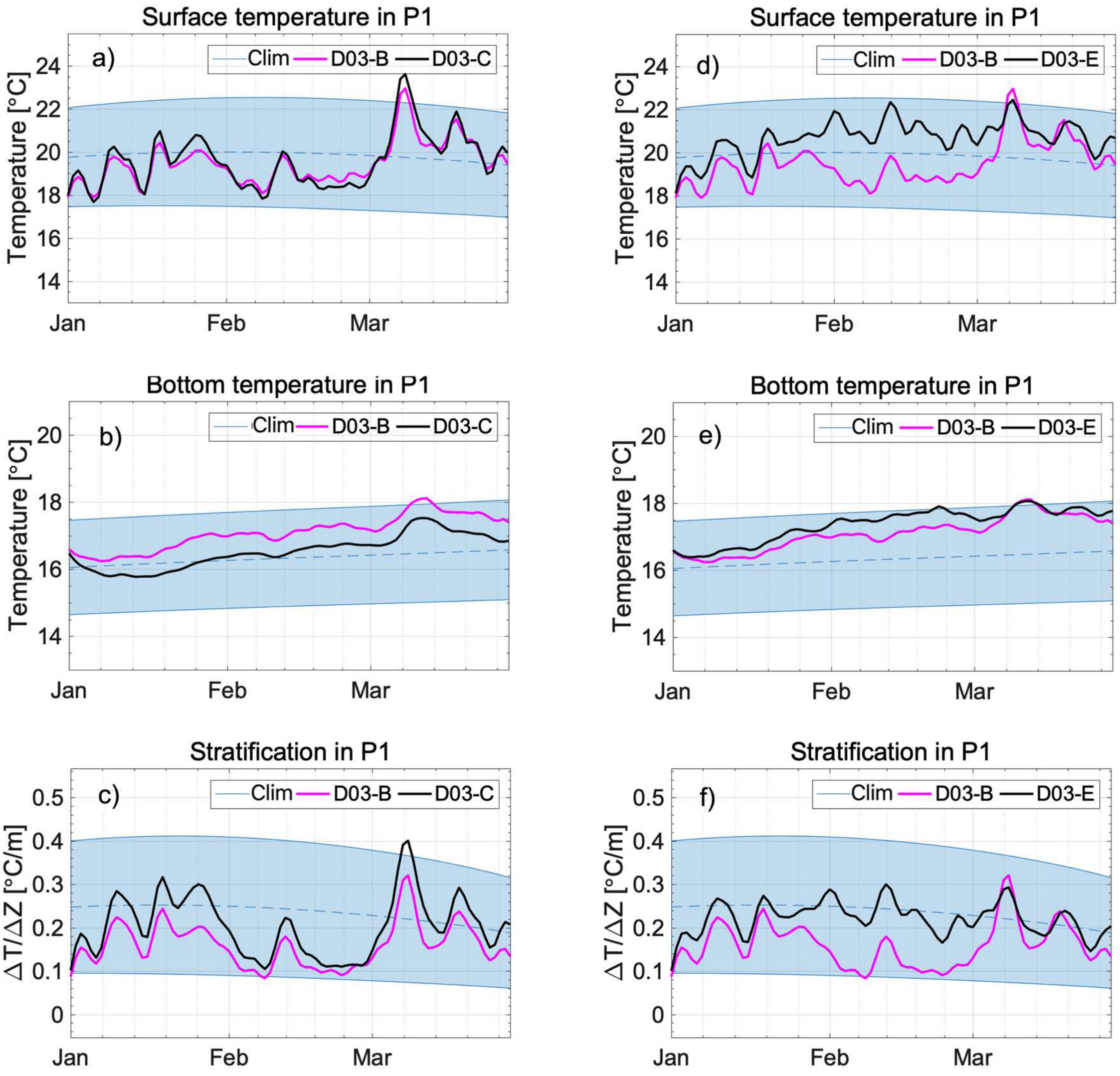

Figure 9: Time series of (a,d) surface, (b,e) bottom and (c,f) thermal stratification (in °C m^{-1}) at P1 from (left) simulations D03-B (magenta line) and D03-C (black line) and (right) D03-B (magenta line) and D03-E (black line). The blue lines and shaded envelopes represent the mean and variability of the observations.

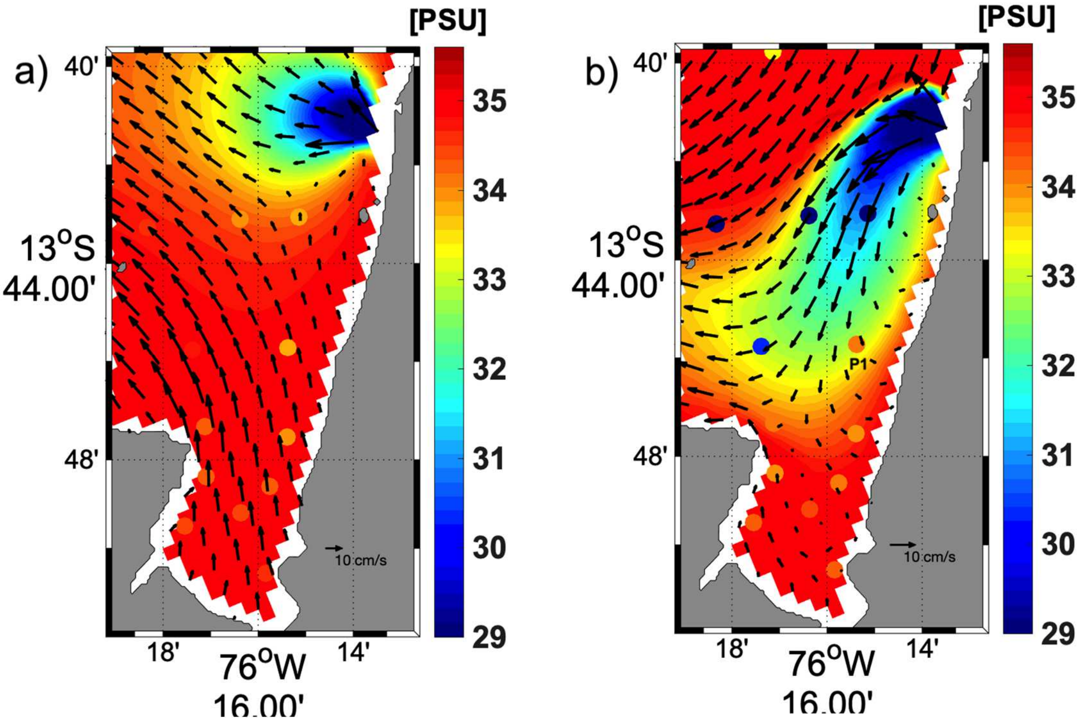

Figure 10: D03-G surface salinity (shading, in psu) and current (vector, in cm s^{-1}) for (a) summer and (b) on the day of weakest wind (early March, see Fig.11a). Colored dots in (a) and (b) show the observed summer averaged salinity and the salinity on 16 February 2011, a weak wind day (4.3 m/s), measured at IMARPE-Pisco laboratory stations.

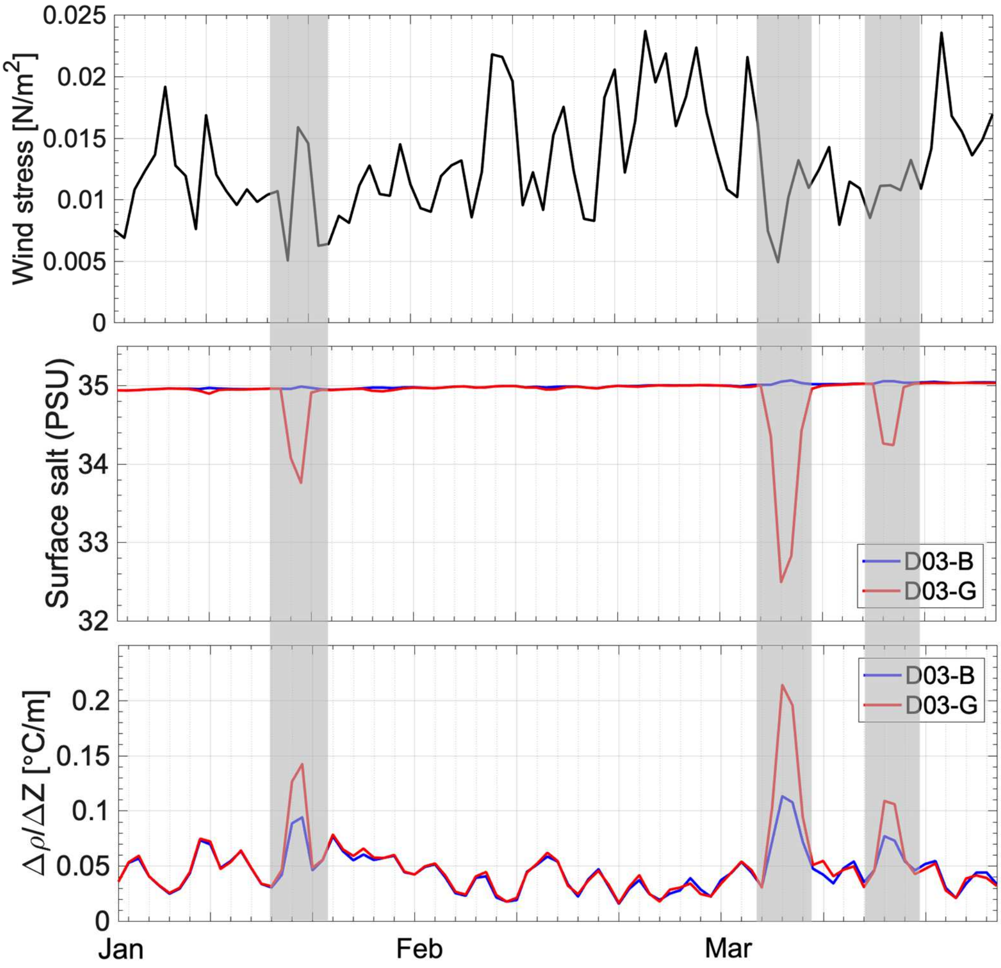

Figure 11: Time series of wind stress (top, in N m^{-2}), surface salinity (middle, in psu) and bottom-surface density stratification (in σ m^{-1}) during January-March at P1 north of the bay. Time series from simulations D03-B and D03-G are marked by blue and red lines, respectively. Grey bars highlight weak wind time periods.

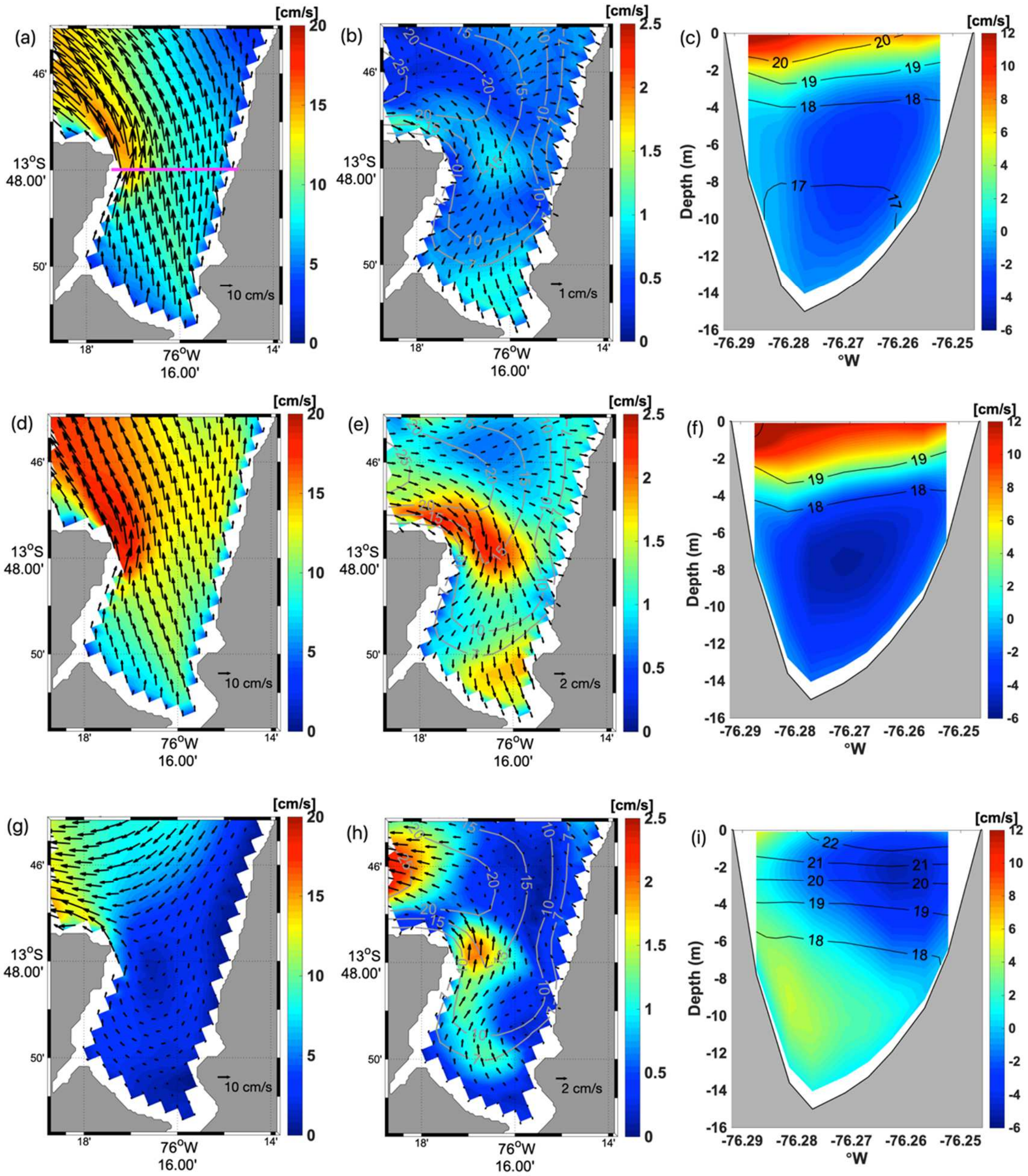

Figure 12: (Top) Summer-averaged currents in (a) surface and (b) bottom layers. (c) Zonal vertical section (indicated by magenta color line in a) of meridional velocity (shading, in m s^{-1}) and temperature (in °C, black lines) at the mouth of the bay. (d-f, middle) same as (a-c) for the day of strongest wind (late March, see red star in Fig.7d). (g-i, bottom) same as (a-c) for the day of weakest wind (early March, see blue star in Fig.7d).

Simulation name	Wind forcing	Wind diurnal cycle	Shortwave absorption depth	tidal forcing	river discharge	solar heat flux bias correction	vertical mixing param.
D03-A	WRF’	no	no	no	no	yes	GLS
D03-B	WRF’	yes	no	no	no	yes	GLS
D03-C	WRF’	yes	yes	no	no	yes	GLS
D03-D	WRF’	yes	no	yes	no	yes	GLS
D03-E	WRF*	yes	no	no	no	yes	GLS
D03-G	WRF’	yes	no	no	yes	yes	GLS
D03-I	WRF*	yes	yes	no	no	yes	GLS

Table 1: Characteristics of the D03 simulations. WRF’ is the daily “climatological” WRF wind, and WRF* is the rescaled WRF’ using ASCAT wind intensity (see section 2.4.b).

Simulation name	All stations Bias/RMSE (10^{-2} σ m^{-1})	northern stations Bias/RMSE (10^{-2} σ m^{-1})	southern stations Bias/RMSE (10^{-2} σ m^{-1})
D03-A (Base experiment)	-5.61/8.53	-4.15/10.60	-1.46/4.70
D03-B (D03-A + DW)	-4.70/8.01	-3.72/10.01	-0.98/4.20
D03-C (D03-A + DW+jwt)	-4.23/7.72	-3.48/9.66	-0.75/4.04
D03-D (D03-A + DW+tide	-5.05/8.24	-3.90/10.30	-1.14/4.34
D03-E(D03-A + DW+WC)	-1.68/6.92	-2.26/8.26	0.57/4.66
D03-G (D03A + DW + river)	-4.21/7.50	-3.37/9.34	-0.83/4.07
D03-I (D03-A + DW+ river)	-1.08/6.86	-1.97/7.96	0.89/5.11

Table 2: Stratification (in σ m^{-1}) bias and root mean square error (RMSE) computed from summer (January-March) IMARPE-Pisco laboratory in situ temperature and salinity and from model output. Northern stations are located north of the bay (1-9) and southern stations are located in the bay (10-16, see Fig.1.b). “DW” means diurnal wind, “jwt” means “Jerlov water type” used for the shortwave absorption depth, “WC” means wind correction.

Simulation name	Temperature stratification at P1 (°C m^{-1})	Average density stratification at P1 (10^{-2} σ m^{-1})	Impact of forcing /parameterization (%)
P1 observations	**0.255**	**6.36**	
D03-A (Base experiment)	0.163	4.1 (1.75 %)	
D03-B (D03-A + DW)	0.191	4.9 (1.72%)	19% (B-A)/A
D03-C (D03-A + DW+jwt)	0.229	5.9 (1.49%)	20% (C-B)/B
D03-D (D03-A + DW+tide)	0.191	4.9 (1.72%)	<1% (D-B)/B
D03-E (D03-A + DW+WC)	0.271	7.1 (1.30%)	44% (E-B)/B
D03-G (D03-A + DW+ river)	0.187	5.4 (15.58%)	10% (G-B)/B
D03-I (D03-A + DW + jwt + WC)	0.334	8.6 (0.65%)	75%(I-B)/B

Table 3 : Impact of the D03 model forcings and parameterizations on the stratification at station P1. The first column indicates the name of the experiment, the second column lists the time-average thermal stratification, the third column lists the time-average density stratification, and the fourth column indicates the impact of each forcing or parameterization, computed as a percentage. In the third column, the observed density difference is computed using a constant salinity (35 psu) due to the absence of salinity measurements at P1. In the model experiments, the density stratification is computed using the modeled salinity. The percentage in the third column indicates the model stratification change obtained with a constant salinity (35 psu). Note that it does not modify significantly the density stratification (less than 2%) except for D03-G including the river discharge (15% increase of stratification when the modeled salinity is used).